JWST sighting of decameter main-belt asteroids and view on meteorite sources

JWST sighting of decameter main-belt asteroids and view on meteorite sources

Artem Y. Burdanov[1,*], Julien de Wit[1,*], Miroslav Brož[2], Thomas G. Müller[3], Tobias Hoffmann[4], Marin Ferrais[5], Marco Micheli[6], Emmanuel Jehin[7], Daniel Parrott[8], Samantha N. Hasler[1], Richard P. Binzel[1], Elsa Ducrot[9], Laura Kreidberg[10], Michaël Gillon[11], Thomas P. Greene[12], Will M. Grundy[13], Theodore Kareta[13], Pierre-Olivier Lagage[9], Nicholas Moskovitz[13], Audrey Thirouin[13], Cristina A. Thomas[14], and Sebastian Zieba[10,15].

[*] *These authors contributed equally to this work.*

[1] *Department of Earth, Atmospheric and Planetary Sciences, Massachusetts Institute of Technology, Cambridge, MA, USA;*

[2] *Charles University, Faculty of Mathematics and Physics, Institute of Astronomy, V Holešovičkách 2, 18000 Prague 8, Czech Republic;*

[3] *Max-Planck-Institut für extraterrestrische Physik, Giessenbachstraße, Postfach 1312, 85741 Garching, Germany;*

[4] *Department of Medical Physics and Acoustics, Carl von Ossietzky University of Oldenburg, 26111 Oldenburg, Germany;*

[5] *Florida Space Institute, University of Central Florida, 12354 Research Parkway, Partnership 1 building, Orlando, FL 32828, USA;*

[6] *ESA PDO NEO Coordination Centre, Largo Galileo Galilei, 1, 00044 Frascati (RM), Italy;*

[7] *Space sciences, Technologies & Astrophysics Research (STAR) Institute University of Liège*

Allée du 6 Août 19, 4000 Liège, Belgium;

[8] *Tycho Tracker, Parrott's Studio, LLC, Oklahoma City, Oklahoma 73179, USA ;*

[9] *Université Paris-Saclay, Université Paris-Cité, CEA, CNRS, AIM, Gif-sur-Yvette, 91191, France;*

[10] *Max-Planck-Institut für Astronomie, Königstuhl 17, D-69117 Heidelberg, Germany;*

[11] *Astrobiology Research Unit, University of Liège Allée du 6 Août 19, 4000 Liège, Belgium;*

[12] *Space Science and Astrobiology Division, NASA's Ames Research Center, M.S. 245-6, Moffett Field, 94035, CA, USA*

[13] *Lowell Observatory, 1400 West Mars Hill Road, Flagstaff, AZ 86001, USA;*

[14] *Northern Arizona University, Department of Astronomy & Planetary Science, PO Box 6010, Flagstaff, AZ 86011, USA;*

[15] *Leiden Observatory, Leiden University, Niels Bohrweg 2, 2333CA Leiden, The Netherlands.*

Asteroid discoveries are essential for planetary-defense efforts aiming to prevent impacts with Earth[1], including the more frequent[2] megaton explosions from decameter impactors[3–6]. While large asteroids ($\geq$100 km) have remained in the main belt since their formation[7], small asteroids are commonly transported to the near-Earth object (NEO) population[8,9]. However, due to the lack of direct observational constraints, their size-frequency distribution —which informs our understanding of the NEOs and the delivery of meteorite samples to Earth—varies significantly among models[10–14]. Here, we report 138 detections of the smallest asteroids ($\gtrapprox$10 m) ever observed in the main belt, which were enabled by

JWST's infrared capabilities covering the asteroids' emission peaks[15] and synthetic tracking techniques[16–18]. Despite small orbital arcs, we constrain the objects' distances and phase angles using known asteroids as proxies, allowing us to derive sizes via radiometric techniques. Their size-frequency distribution exhibits a break at $\sim 100\,\mathrm{m}$ (debiased cumulative slopes of $q = -2.66 \pm 0.60$ and -0.97 ± 0.14 for diameters smaller and larger than $\sim$100 m, respectively), suggestive of a population driven by collisional cascade. These asteroids were sampled from multiple asteroid families —most likely Nysa, Polana and Massalia— according to the geometry of pointings considered here. Through additional long-stare infrared observations, JWST is poised to serendipitously detect thousands of decameter-scale asteroids across the sky, probing individual asteroid families[19] and the source regions of meteorites[13,14] "in-situ".

1 Main

An edge from synthetic-tracking and infrared Asteroids are discovered by their motion relative to the background stars. This observed motion results from asteroids' actual orbital movement combined with motion induced by Earth's (and/or a satellite's) parallactic movement. While most asteroid-search projects detect objects in single images (exposures) and link their motion across multiple images, this method may miss fainter objects which are not visible on an individual image. To address this, the "shift-and-stack" technique, developed in the 1990s, enhances the signal-to-noise ratio (SNR) by combining multiple images into one

"stack" image[16,20,21]. This method involves predicting the asteroid's motion, shifting image pixels accordingly, and then combining the images (Fig. 1). Synthetic tracking, an extension of "shift-and-stack" technique, does not rely on prior knowledge of an asteroid's motion, but rather performs a fully "blind" search by testing a series of possible shifts[17,22,23] (i.e., velocity vectors). However, this method's computational intensity posed a bottleneck until the widespread availability of graphics processing units (GPUs). The subsequent usage of GPU-based synthetic tracking increases the scientific return of monitory campaigns, such as exoplanet transit-search surveys, by recovering serendipitous asteroid detections[18,24].

The vast majority of known asteroids have been discovered by ground-based surveys at visible wavelengths. Asteroids' full spectral energy distributions are a combination of reflected sunlight (driven by the object's albedo) and thermal emission, with the central wavelengths of the thermal peak ranging between 5 and 20 μm for objects between 1 and 10 au (Fig. 2). With an exquisite sensitivity in that wavelength range and a large aperture, JWST is ideal for detecting the thermal emission of asteroids and revealing the smallest main-belt asteroids (MBAs)[15]. Such observations combined with orbital information can yield accurate radius estimates, which are less affected by degeneracy with the albedo than those from visible-light observations[25–27]. Indeed, the visible-light detection of a typical MBA with known orbit can be explained by an object with a small size with high albedo or a large size with low albedo. For the wide range of albedos from 3-40%, the corresponding sizes can vary by a factor 3-4. In contrast, a thermal infrared (IR) measurement close to the object's thermal peak constrains the object's size to within

about 10-20% (see Methods).

JWST's potential and decameter delivering JWST observing programs conducted with no dithering are especially suitable for synthetic tracking as all exposures from one visit can be shifted and stacked. This makes JWST sensitive to small IR fluxes from moving objects in a field of view (FoV) and enhances its capability to detect faint asteroids. Such a dithering-free long-stare mode was used to observe the TRAPPIST-1 star (located 0.6 deg from the ecliptic) with the MIRI instrument[28] at 15 μm as part of multiple programs aimed at characterizing the TRAPPIST-1 exoplanetary system through measurements of the inner planets' day-side emission (Program IDs 1177 and 2304, with Greene, and Kreidberg as PI, respectively) and their combined thermal phase curve (PID 3077, PI Gillon). In total, JWST observed the TRAPPIST-1 star for 93.5 hours during 11 visits in 2022-2023. After applying our GPU-based framework for detecting asteroids in targeted exoplanet surveys[18,24], we were able to detect 8 known and 138 unknown asteroids which happened to serendipitously cross MIRI FoV of $56.3'' \times 56.3''$ or $112'' \times 113''$ (depending on the particular observing program). The known objects are MBAs with fluxes between 100 and 1,700 μJy and diameters (D) between 200 and 2,500 m (Extended Data Table 1).

The 138 new detections could not be attributed to any known asteroids, where we searched for previously discovered objects positioned closer than 1' from each detection (see Methods). IR fluxes of these new objects range from 0.5 μJy to 600 μJy, with a detection/sensitivity thresh-

old at $\sim 0.5\,\mu$Jy (see Methods and Extended Data Figure 1). Our detections spend from 30 min to 8 hours in the MIRI FoV. Even in the case of the longest observing arc of 8 hours, orbits of different dynamical classes can fit the data well and are statistically indistinguishable. We thus used ensembles of known objects which were predicted to be in a $6^\circ \times 2^\circ$ area around the TRAPPIST-1 star at the time of detection of an unknown asteroid as proxies to derive posterior probability distributions on the distance from JWST to each unknown asteroid (see example in Extended Data Figure 2). This methodology yielded the distance with a typical uncertainty of $\sim$0.2 au and adequately returned the distance of the eight known asteroids (see Methods, and Extended Data Figure 3). We estimated distances from JWST to unknown asteroids to be from 0.9 to 3.0 au placing them primarily in the main asteroid belt, with diameters ranging from 10 to 500 m (see Fig. 3 and Methods). Amongst them six appear associated with the population of near-Earth objects (marked as "NEOs?" in Fig. 3), and one with the population of Trojans (see Methods and Extended Data Table 2). The detection/sensitivity threshold at $\sim$0.5 μJy starts at $\sim$1.5 μJy and translates into an observational bias emerging in the 20- to 40-m diameter regime with a sharp cutoff by $\sim$10 m (Extended Data Figure 1).

Population statistics and possible origins The size-frequency distribution (SFD) of our asteroid detections is unusually shallow at sizes larger than $\sim$100 m, corresponding to a population depleted by collisions (Fig. 4). It can be described by a power law, $N(>D) = CD^q$, with the exponent $q = -0.97 \pm 0.14$. This exponent is derived from the debiased SFD, i.e., the observed SFD corrected for the size-dependent recovery rate and the non-negligible uncertainties of in-

dividual size estimates (see Methods). On the other hand, the observed SFD is significantly steeper below 100 m, with a debiased exponent $q = -2.66 \pm 0.60$, valid between 100 m and approximately 10 m. The larger uncertainty associated with the steeper part of the SFD is due to the large uncertainties on the sizes ($\sim 25\%$)—primarily driven up by the orbital-configuration uncertainty—that result in a wide range of steep SFDs matching the observed size distribution (see Extended Data Figure 6).

This steeper slope is characteristic of the strength regime of fragmentation[29]. In fact, bodies $\sim 100\,\mathrm{m}$ in size are among the weakest in the Solar System[30]. Their studies thus provide unique insights into realistic asteroidal materials.

At decameter sizes, small bodies are most likely fragments of bigger bodies, linked to recent disruptions and known asteroid families[13,19]. The associations of unknown asteroids are based on the same methodology; on orbits of known objects located close to the JWST field of view (Extended Data Figure 7). More specifically, the Nysa family was sampled, together with Polana, Massalia, Koronis2, and/or Karin (Supplementary Table 1). In particular, the synthetic size-frequency distribution (SFD) of the Nysa and Polana families exhibit similar slopes that match the observations in both the shallow and steep regimes (Extended Data Figure 8). According to the collisional model from ref. [31], their ages are of the order of 200 and 600 My, respectively. Consequently, sub-km bodies should be in a collisional equilibrium. Other families exhibit a variety of slopes, especially because some of them are young[13]. At the decameters

sizes, we expect the Massalia family is dominant since it is the source of the most common meteorites[14]. Nonetheless, when asteroids are sampled from multiple families, the resulting SFD is indeed a combination of steep and shallow slopes, resembling the distribution of the whole asteroid belt (Fig. 4).

Compared to previous pencil-beam surveys[32–35], our observations reveal on one hand a continuation of the shallow slope down to much smaller sizes than previously thought (Fig. 3.b). For example, observations obtained by the Hubble Space Telescope[35] were only complete to V$\sim$23 mag, corresponding to approximately $500\,\mathrm{m}$, and reaching as far as V$\sim$28 mag, similarly as the deepest ground-based observations[6]. On the other hand, when debiasing the JWST observations, we find the slope is steeper than previously thought, with a clear slope increase around 100 m. It is suggestive of the first and long-awaited evidence of a population, which is evolving by collisions and at the same time moving from the main belt to the NEO space.[12]

Since the transport itself is size-dependent due to the Yarkovsky effect[36], the YORP effect[37], or thermal disruptions[38], the SFD of NEOs is substantially different from its source region. Observations of more than 30000 NEOs[11,12] confirm a slope transition at $\sim$100 m. Since the slopes in the NEO region are already known ($q = 2.83 \pm 0.04$ and 1.64 ± 0.02; according to ref. [39]), JWST observations offer the prospect of finally constraining transport mechanisms.

Prospects and planetary-defense efforts Looking ahead, it is anticipated that JWST will be observing 15-20 exoplanet host stars for at least 500 hours with MIRI[40]—a first step on the

roadmap for the atmospheric characterization of (warm) terrestrial exoplanets[41], following a similar observing strategy to the one followed to acquire the data used here[42,43]. As a large fraction of the host stars amenable for such studies are fortuitously found within 20 degrees of the ecliptic, these 500 hours will yield hundreds of additional decameter asteroids. In addition, an average of $\sim$1800 hours of MIRI observations were gathered per Cycle in Cycles 1 through 3. We thus expect that JWST will detect thousands of decameter asteroids per Cycle. Such a substantial increase in sample size—especially if combined with a multi-visit observation strategy to recover orbits precisely and multi-band observations to constrain the thermal and rotation properties of the objects—will reduce significantly the uncertainties on the SFD slope, allowing to disentangle between different families and study the source regions of meteorites[13,14,31] "in-situ".

Beyond the detection of asteroids otherwise undetectable, JWST can also yield exquisite infrared rotation curves of large (i.e., $\gtrapprox$300 m) asteroids thereby allowing their further characterization (see Extended Data Figure 4). The insights gained from JWST's infrared rotation curves of asteroids will be particularly valuable in two ways. First, their precision vastly exceeds their counterpart in the visible. Second, unlike visible rotation curves they are mostly insensitive to surface topology—which results in reduced degeneracy with the albedo (similarly to the size-estimation process in the infrared). As rotation rates can inform the origin and evolution of asteroid family[44–46], their relationship to the break-up barrier[47], and even be used to derive their internal properties during close encounters[48] JWST is also poised to further our

understanding of asteroid families and meteorite source bodies through rotation measurements.

There is thus a great deal of synergy between JWST and other facilities dedicated to the study of minor bodies, such as the Rubin observatory[49]—an all-sky survey in the visible aiming at discoveries of 100-meter asteroids—and the Near-Earth Object Surveyor mission[50] with its unprecedented potential for the discovery and characterization of NEOs. Combining the expected discoveries of such dedicated facilities with the capabilities of JWST presented here will finally allow to constrain dynamical and collisional models all the way down to 10 m.

This synergy will extend beyond scientific endeavors and support planetary-defense efforts. Although planetary-defense often appears associated with preventing events such as the impact that led to the extinction of the dinosaurs[51], decameter objects offer non-negligible threats which occur at much higher rates—rates are proportional to $D^{-2.7}$, leading to decameter impactors being $\sim$10,000 times more frequent than km-sized ones[2]. Decameter objects can lead to megaton explosions leaving behind km-sized craters. They are in fact at the origin of relatively recent events of importance on Earth like Chelyabinsk[10], Tunguska[3], Barringer[4], or Steinheim[5]. JWST's capability to observe decameter objects all the way to the main belt (incl. NEOs at their aphelion) while deriving tighter (i.e., nearly albedo-independent) sizes highlights its unique capability to monitor and study with exquisite precision possible future impactors detected closer to Earth by other surveys, thereby making JWST an important asset for future planetary-defense efforts.

2 References Main Text

1. Cheng, A. F. *et al.* AIDA DART asteroid deflection test: Planetary defense and science objectives. *Planetary Space Science* **157**, 104–115 (2018).

2. Brown, P., Spalding, R. E., ReVelle, D. O., Tagliaferri, E. & Worden, S. P. The flux of small near-Earth objects colliding with the Earth. *Nature* **420**, 294–296 (2002).

3. Chyba, C. F., Thomas, P. J. & Zahnle, K. J. The 1908 Tunguska explosion: atmospheric disruption of a stony asteroid. *Nature* **361**, 40–44 (1993).

4. Chao, E. C. T., Shoemaker, E. M. & Madsen, B. M. First Natural Occurrence of Coesite. *Science* **132**, 220–222 (1960).

5. Stöffler, D., Artemieva, N. A. & Pierazzo, E. Modeling the Ries-Steinheim impact event and the formation of the moldavite strewn field. *Meteor. Planet. Sci.* **37**, 1893–1907 (2002).

6. Reddy, V. *et al.* Near-Earth asteroid 2012 TC4 observing campaign: Results from a global planetary defense exercise. *Icarus* **326**, 133–150 (2019).

7. Bottke, W. F. *et al.* The fossilized size distribution of the main asteroid belt. *Icarus* **175**, 111–140 (2005).

8. Farinella, P., Vokrouhlický, D. & Hartmann, W. K. Meteorite Delivery via Yarkovsky Orbital Drift. *Icarus* **132**, 378–387 (1998).

9. Chesley, S. R. *et al.* Direct Detection of the Yarkovsky Effect by Radar Ranging to Asteroid 6489 Golevka. *Science* **302**, 1739–1742 (2003).

10. Brown, P. G. *et al.* A 500-kiloton airburst over Chelyabinsk and an enhanced hazard from small impactors. *Nature* **503**, 238–241 (2013).

11. Harris, A. W. & Chodas, P. W. The population of near-earth asteroids revisited and updated. *Icarus* **365**, 114452 (2021).

12. Nesvorný, D. *et al.* NEOMOD 2: An updated model of Near-Earth Objects from a decade of Catalina Sky Survey observations. *Icarus* **411**, 115922 (2024). 2312.09406.

13. Brož, M. *et al.* Young asteroid families as the primary source of meteorites. *Nature* **634**, 566–571 (2024). 2403.08552.

14. Marsset, M. *et al.* The Massalia asteroid family as the origin of ordinary L chondrites. *Nature* **634**, 561–565 (2024). 2403.08548.

15. Müller, T. G. *et al.* Asteroids seen by JWST-MIRI: Radiometric size, distance, and orbit constraints. *Astron. Astrophys.* **670**, A53 (2023). 2302.06921.

16. Tyson, J., Guhathakurta, P., Bernstein, G. & Hut, P. Limits on the surface density of faint kuiper belt objects. In *American Astronomical Society Meeting Abstracts*, vol. 181, 06–10 (1992).

17. Shao, M. *et al.* Finding very small near-earth asteroids using synthetic tracking. *Astrophys. J.* **782**, 1 (2014).

18. Burdanov, A. Y., Hasler, S. N. & de Wit, J. GPU-based framework for detecting small Solar system bodies in targeted exoplanet surveys. *Mon. Not. R. Astron. Soc.* **521**, 4568–4578 (2023). 2303.07293.

19. Nesvorný, D., Brož, M. & Carruba, V. Identification and Dynamical Properties of Asteroid Families. In Michel, P., DeMeo, F. E. & Bottke, W. F. (eds.) *Asteroids IV*, 297–321 (Univ. Arizona Press, 2015).

20. Gladman, B. & Kavelaars, J. J. Kuiper Belt searches from the Palomar 5-m telescope. *Astron. Astrophys.* **317**, L35–L38 (1997). astro-ph/9610150.

21. Bernstein, G. M. *et al.* The Size Distribution of Trans-Neptunian Bodies. *Astron. J.* **128**, 1364–1390 (2004). astro-ph/0308467.

22. Zhai, C. *et al.* Detection of a Faint Fast-moving Near-Earth Asteroid Using the Synthetic Tracking Technique. *Astrophys. J.* **792**, 60 (2014). 1403.4353.

23. Heinze, A. N., Metchev, S. & Trollo, J. Digital Tracking Observations Can Discover Asteroids 10 Times Fainter Than Conventional Searches. *Astron. J.* **150**, 125 (2015). 1508.01599.

24. Hasler, S. N. *et al.* Small body harvest with the Antarctic Search for Transiting Exoplanets (ASTEP) project. *Mon. Not. R. Astron. Soc.* **526**, 3601–3609 (2023). 2309.14180.

25. Tedesco, E. F., Noah, P. V., Noah, M. & Price, S. D. The Supplemental IRAS Minor Planet Survey. *Astron. J.* **123**, 1056–1085 (2002).

26. Usui, F. *et al.* Asteroid Catalog Using Akari: AKARI/IRC Mid-Infrared Asteroid Survey. *Publications of the Astronomical Society of Japan* **63**, 1117–1138 (2011).

27. Mainzer, A. *et al.* Preliminary Results from NEOWISE: An Enhancement to the Wide-field Infrared Survey Explorer for Solar System Science. *Astrophys. J.* **731**, 53 (2011). 1102.1996.

28. Rieke, G. H. *et al.* The Mid-Infrared Instrument for the James Webb Space Telescope, VII: The MIRI Detectors. *Publ. Astron. Soc. Pacific* **127**, 665 (2015). 1508.02362.

29. Dohnanyi, J. S. Collisional Model of Asteroids and Their Debris. *Journal of Geophysics Research* **74**, 2531–2554 (1969).

30. Benz, W. & Asphaug, E. Catastrophic Disruptions Revisited. *Icarus* **142**, 5–20 (1999). arXiv:astro-ph/9907117.

31. Brož, M. *et al.* Source regions of carbonaceous meteorites and near-Earth objects. *Astron. Astrophys.* **689**, A183 (2024). 2406.19727.

32. Gladman, B. J. *et al.* On the asteroid belt's orbital and size distribution. *Icarus* **202**, 104–118 (2009).

33. Ryan, E. L. *et al.* The kilometer-sized Main Belt asteroid population revealed by Spitzer. *Astron. Astrophys.* **578**, A42 (2015).

34. Maeda, N. *et al.* Size Distributions of Bluish and Reddish Small Main-belt Asteroids Obtained by Subaru/Hyper Suprime-Cam. *Astron. J.* **162**, 280 (2021). 2110.00178.

35. García-Martín, P. *et al.* Hubble Asteroid Hunter. III. Physical properties of newly found asteroids. *Astron. Astrophys.* **683**, A122 (2024). 2401.02605.

36. Vokrouhlický, D. A complete linear model for the Yarkovsky thermal force on spherical asteroid fragments. *Astron. Astrophys.* **344**, 362–366 (1999).

37. Rubincam, D. P. Radiative Spin-up and Spin-down of Small Asteroids. *Icarus* **148**, 2–11 (2000).

38. Granvik, M. *et al.* Super-catastrophic disruption of asteroids at small perihelion distances. *Nature* **530**, 303–306 (2016).

39. Nesvorný, D. *et al.* NEOMOD: A New Orbital Distribution Model for Near-Earth Objects. *Astron. J.* **166**, 55 (2023). 2306.09521.

40. Redfield, S. *et al.* Report of the Working Group on Strategic Exoplanet Initiatives with HST and JWST. *arXiv e-prints* arXiv:2404.02932 (2024). 2404.02932.

41. TRAPPIST-1 JWST Community Initiative, J., de Wit *et al.* A roadmap for the atmospheric characterization of terrestrial exoplanets with JWST. *Nature Astronomy* **8**, 810–818 (2024). 2310.15895.

42. Greene, T. P. *et al.* Thermal emission from the Earth-sized exoplanet TRAPPIST-1 b using JWST. *Nature* **618**, 39–42 (2023). 2303.14849.

43. Zieba, S. *et al.* No thick carbon dioxide atmosphere on the rocky exoplanet TRAPPIST-1 c. *Nature* **620**, 746–749 (2023). 2306.10150.

44. Farinella, P., Davis, D. R., Paolicchi, P., Cellino, A. & Zappala, V. Asteroid collisional evolution - an integrated model for the evolution of asteroid rotation rates. *Astron. Astrophys.* **253**, 604–614 (1992).

45. Bottke, J., William F., Vokrouhlický, D., Rubincam, D. P. & Nesvorný, D. The Yarkovsky and Yorp Effects: Implications for Asteroid Dynamics. *Annual Review of Earth and Planetary Sciences* **34**, 157–191 (2006).

46. Carruba, V. *et al.* The population of rotational fission clusters inside asteroid collisional families. *Nature Astronomy* **4**, 83–88 (2020).

47. Polishook, D. Spin axes and shape models of asteroid pairs: Fingerprints of YORP and a path to the density of rubble piles. *Icarus* **241**, 79–96 (2014). 1406.3359.

48. Dinsmore, J. T. & de Wit, J. Constraining the interiors of asteroids through close encounters. *Mon. Not. R. Astron. Soc.* **520**, 3459–3475 (2023). 2210.10754.

49. LSST Science Collaboration *et al.* LSST Science Book, Version 2.0. *arXiv e-prints* arXiv:0912.0201 (2009). 0912.0201.

50. Mainzer, A. K. *et al.* The Near-Earth Object Surveyor Mission. *Planetary Science Journal* **4**, 224 (2023). 2310.12918.

51. Alvarez, L. W., Alvarez, W., Asaro, F. & Michel, H. V. Extraterrestrial Cause for the Cretaceous-Tertiary Extinction. *Science* **208**, 1095–1108 (1980).

52. Metropolis, N. & Ulam, S. The monte carlo method. *Journal of the American Statistical Association* **44**, 335–341 (1949). URL http://www.jstor.org/stable/2280232.

53. Bradley, L. *et al.* astropy/photutils: 1.8.0 (2023). URL https://doi.org/10.5281/zenodo.7946442.

54. Parrott, D. Tycho tracker: A new tool to facilitate the discovery and recovery of asteroids using synthetic tracking and modern gpu hardware. *Journal of the American Association of Variable Star Observers (JAAVSO)* **48**, 262 (2020).

55. Greene, T. P. *et al.* Thermal emission from the Earth-sized exoplanet TRAPPIST-1 b using JWST. *Nature* **618**, 39–42 (2023). 2303.14849.

56. Brown, M. E., Kulkarni, S. R. & Liggett, T. J. An Analysis of the Statistics of the Hubble Space Telescope Kuiper Belt Object Search. *Astrophys. J., Letters* **490**, L119–L122 (1997).

57. Cochran, A. L., Levison, H. F., Tamblyn, P., Stern, S. A. & Duncan, M. J. The Calibration of the Hubble Space Telescope Kuiper Belt Object Search: Setting the Record Straight. *Astrophys. J., Letters* **503**, L89–L93 (1998). astro-ph/9806210.

58. Hoffmann, T. *et al.* Debiasing astro-Photometric Observations with Corrections Using Statistics (DePhOCUS). *arXiv e-prints* arXiv:2408.07474 (2024). 2408.07474.

59. Harris, A. W. A Thermal Model for Near-Earth Asteroids. *Icarus* **131**, 291–301 (1998).

60. Masiero, J. R. *et al.* Main Belt Asteroids with WISE/NEOWISE. I. Preliminary Albedos and Diameters. *Astrophys. J.* **741**, 68 (2011). 1109.4096.

61. Alí-Lagoa, V. & Delbo', M. Sizes and albedos of Mars-crossing asteroids from WISE/NEOWISE data. *Astron. Astrophys.* **603**, A55 (2017). 1705.10263.

62. Alí-Lagoa, V., Müller, T. G., Usui, F. & Hasegawa, S. The AKARI IRC asteroid flux catalogue: updated diameters and albedos. *Astron. Astrophys.* **612**, A85 (2018). 1712.07496.

63. Wolters, S. D., Green, S. F., McBride, N. & Davies, J. K. Thermal infrared and optical observations of four near-Earth asteroids. *Icarus* **193**, 535–552 (2008).

64. Mainzer, A. *et al.* NEOWISE Observations of Near-Earth Objects: Preliminary Results. *Astrophys. J.* **743**, 156 (2011). 1109.6400.

65. Grav, T. *et al.* WISE/NEOWISE Observations of the Hilda Population: Preliminary Results. *Astrophys. J.* **744**, 197 (2012). 1110.0283.

66. Vilenius, E. *et al.* "TNOs are Cool": A survey of the trans-Neptunian region. VI. Herschel/PACS observations and thermal modeling of 19 classical Kuiper belt objects. *Astron. Astrophys.* **541**, A94 (2012). 1204.0697.

67. Pravec, P. & Harris, A. W. Fast and Slow Rotation of Asteroids. *Icarus* **148**, 12–20 (2000).

68. Lebofsky, L. A. & Spencer, J. R. Radiometry and thermal modeling of asteroids. In Binzel, R. P., Gehrels, T. & Matthews, M. S. (eds.) *Asteroids II*, 128–147 (1989).

69. Harris, A. W. & Lagerros, J. S. V. Asteroids in the Thermal Infrared. In *Asteroids III*, 205–218 (2002).

70. Mainzer, A. *et al.* The Population of Tiny Near-Earth Objects Observed by NEOWISE. *Astrophys. J.* **784**, 110 (2014). 1310.2980.

71. Fenucci, M., Novaković, B. & Marčeta, D. The low surface thermal inertia of the rapidly rotating near-Earth asteroid 2016 GE1. *Astron. Astrophys.* **675**, A134 (2023). 2306.07693.

72. DeMeo, F. E. & Carry, B. Solar System evolution from compositional mapping of the asteroid belt. *Nature* **505**, 629–634 (2014). 1408.2787.

73. Burdanov, A. Y. *et al.* SPECULOOS Northern Observatory: Searching for Red Worlds in the Northern Skies. *Publ. Astron. Soc. Pacific* **134**, 105001 (2022). 2209.09112.

74. Delrez, L. *et al.* SPECULOOS: a network of robotic telescopes to hunt for terrestrial planets around the nearest ultracool dwarfs. In Marshall, H. K. & Spyromilio, J. (eds.) *Ground-based and Airborne Telescopes VII*, vol. 10700 of *Society of Photo-Optical Instrumentation Engineers (SPIE) Conference Series*, 107001I (2018). 1806.11205.

75. Jehin, E. *et al.* Trappist: Transiting planets and planetesimals small telescope. *The Messenger* **145**, 2–6 (2011).

76. Mommert, M. PHOTOMETRYPIPELINE: An automated pipeline for calibrated photometry. *Astronomy and Computing* **18**, 47–53 (2017). 1702.00834.

77. Levine, S. E. *et al.* Status and performance of the Discovery Channel Telescope during commissioning. In Stepp, L. M., Gilmozzi, R. & Hall, H. J. (eds.) *Ground-based and Airborne Telescopes IV*, vol. 8444 of *Society of Photo-Optical Instrumentation Engineers (SPIE) Conference Series*, 844419 (2012).

78. Harris, C. R. *et al.* Array programming with NumPy. *Nature* **585**, 357–362 (2020). URL https://doi.org/10.1038/s41586-020-2649-2.

79. Hunter, J. D. Matplotlib: A 2d graphics environment. *Computing in Science & Engineering* **9**, 90–95 (2007).

80. Astropy Collaboration *et al.* Astropy: A community Python package for astronomy. *Astron. Astrophys.* **558**, A33 (2013). 1307.6212.

81. Astropy Collaboration *et al.* The Astropy Project: Building an Open-science Project and Status of the v2.0 Core Package. *Astron. J.* **156**, 123 (2018). 1801.02634.

82. Virtanen, P. *et al.* SciPy 1.0: Fundamental Algorithms for Scientific Computing in Python. *Nature Methods* **17**, 261–272 (2020).

83. development team, T. P. pandas-dev/pandas: Pandas (2020). URL https://doi.org/10.5281/zenodo.3509134.

84. Wes McKinney. Data Structures for Statistical Computing in Python. In Stéfan van der Walt & Jarrod Millman (eds.) *Proceedings of the 9th Python in Science Conference*, 56 – 61 (2010).

85. Ginsburg, A. *et al.* astroquery: An Astronomical Web-querying Package in Python. *Astron. J.* **157**, 98 (2019). 1901.04520.

86. Christensen, E. J. *et al.* Status of the Catalina Sky Survey. In *LPI Contributions*, vol. 2851 of *LPI Contributions*, 2587 (2023).

3 Main Figures

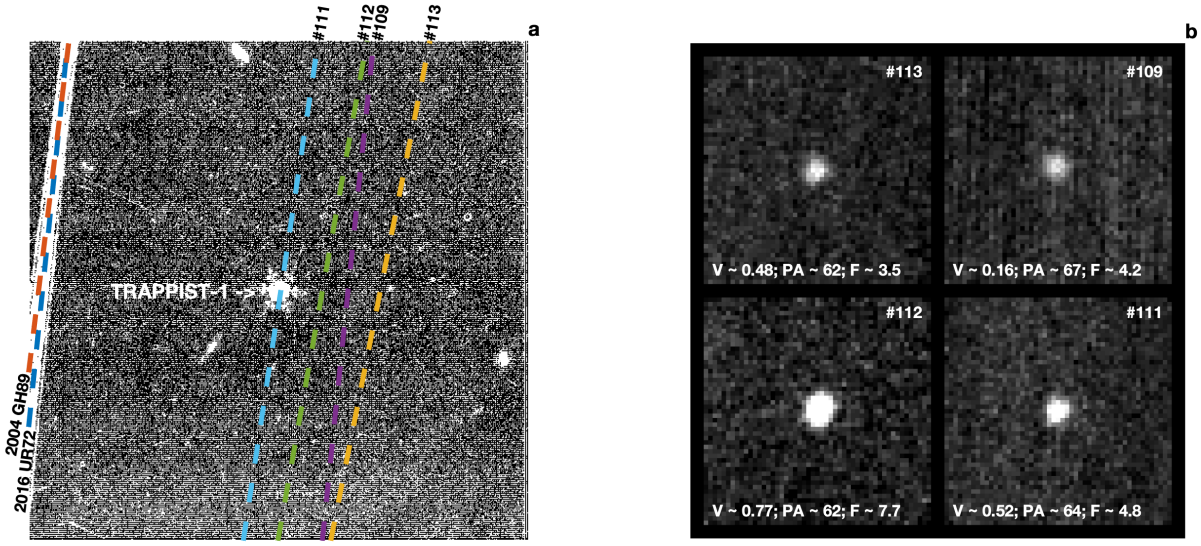

Figure 1: Basics of a blind search for asteroids using synthetic tracking. a. Average stack of exposures 4,000 to 4,500 from PID 3077 centered on the ultra-cool star TRAPPIST-1, revealing two known bright asteroids (2004 GH89 and 2016 UR72) crossing the left side of the field of view (FoV). Being bright, they are detectable on individual exposures, leading to a trail on the stacked exposure. The other dashed lines refer to the paths of four unknown asteroids crossing the FoV at the same time, but only detectable in stacked exposures that are first shifted along their respective paths, which are identified via a blind search through the "shift-and-stack" technique. **b.** Shifted-and-stacked exposures centered on four new asteroids (#113, #109, #112, and #111) with their speed (V, in arcsec/min), position angle (PA, in degree), and Flux (F, in μJy). All the properties of the 138 new asteroids are reported in Supplementary Table 1, and their shifted-and-stacked exposures in Supplementary Figure 1.

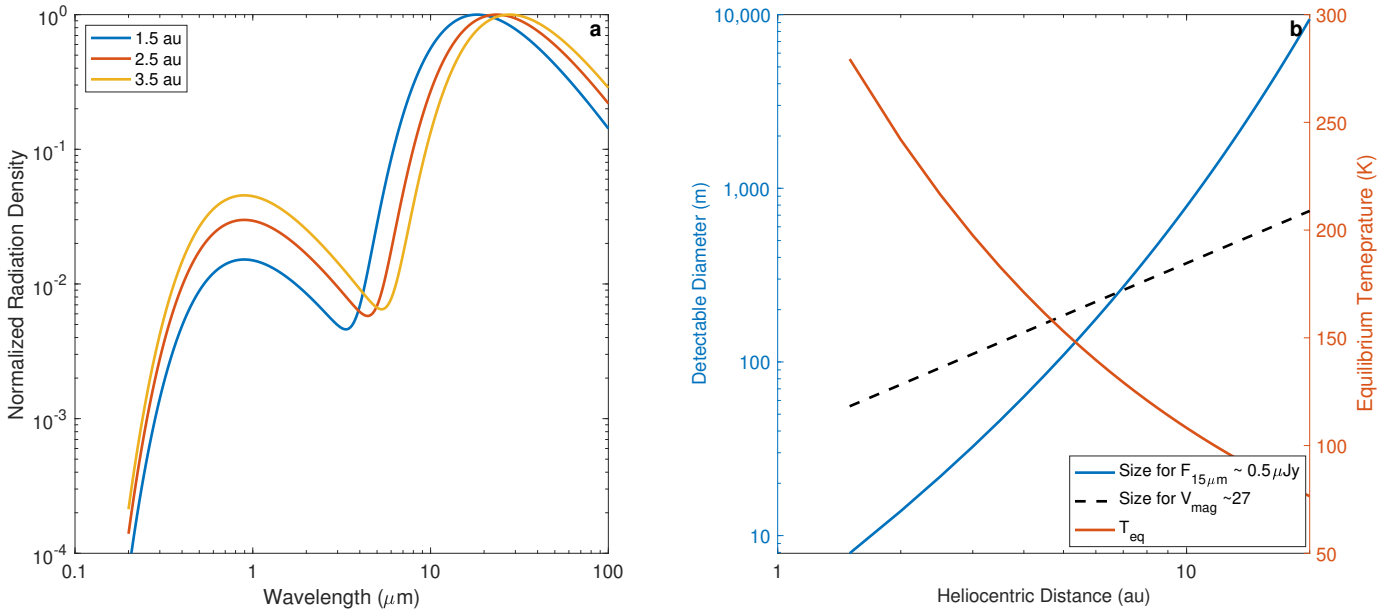

Figure 2: JWST's far-infrared window into the main-belt asteroid population. a. Radiation Density (Jy) normalized to the peak emission for 0.1-albedo asteroids with an heliocentric distance of 1.5 (blue), 2.5 (red), and 3.5 au (yellow) showcasing the favorable infrared-to-visible flux ratio. **b.** Minimum size of an asteroid detectable for a 0.5 μJy detection threshold at 15 μm compared to state-of-the-art capabilities in the visible—dashed line represents the radius detection threshold at Vmag$\sim$27 (ref. [6]). With a 0.5 μJy detection threshold (Extended Data Figure 1), JWST can outperform searches in the visible up to 10 au, and by up to two orders of magnitude in size in the main belt.

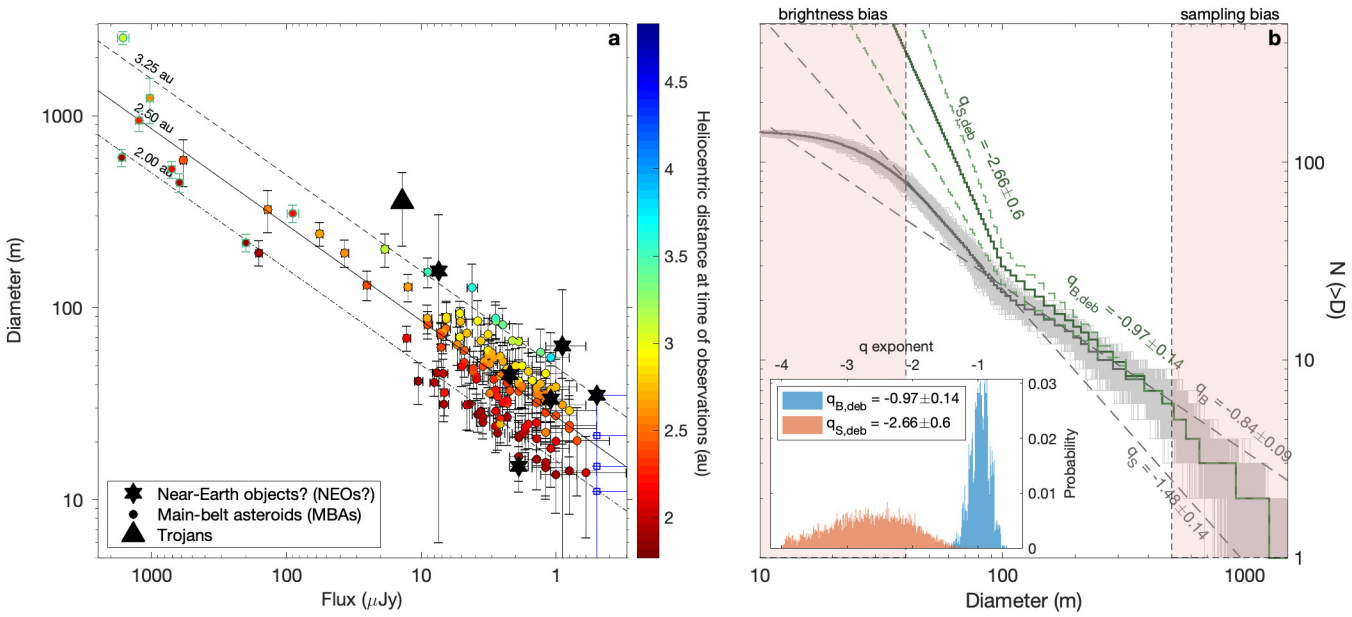

Figure 3: Flux-diameter and size-frequency relationships for the 146 asteroids detected with JWST/MIRI. a. Fluxes, diameters, and heliocentric distances of the detected asteroids. The dash-dot, solid, and dotted lines represent the size-flux relationships for objects at 2.00, 2.50, and 3.25 au, respectively. Known asteroids (green) have smaller size uncertainties thanks to known orbital configurations. Detections beyond the sensitivity threshold ($\sim 0.5\,\mu$Jy, see Extended Data Figure 3) are reported as upper limits on brightness and size via blue empty symbols (see bottom right corner). **b.** Ensemble of cumulative size-frequency distributions (SFDs) built from 1,000 perturbed asteroid diameters in order to propagate the size uncertainties onto the SFD estimate (grey) via the Monte Carlo method[52] together with the debiased SFDs (green)—see Methods for details. Median raw and debiased SFDs are shown as solid lines. The debiased SFD presents two distinct regimes with exponents $q_{S,deb} = -2.66 \pm 0.60$ for small sizes and $q_{B,deb} = -0.97 \pm 0.14$ for big sizes (1-σ interval between green dashed lines, probability distributions in inset)—$N(>D) = CD^q$, transition at $\sim$100 m. The latter is consistent with ref. [34], reporting $q = -1.05 \pm 0.05$. Exponents prior to debiasing the SFDs for the size uncertainties are shown in the bottom right corner.

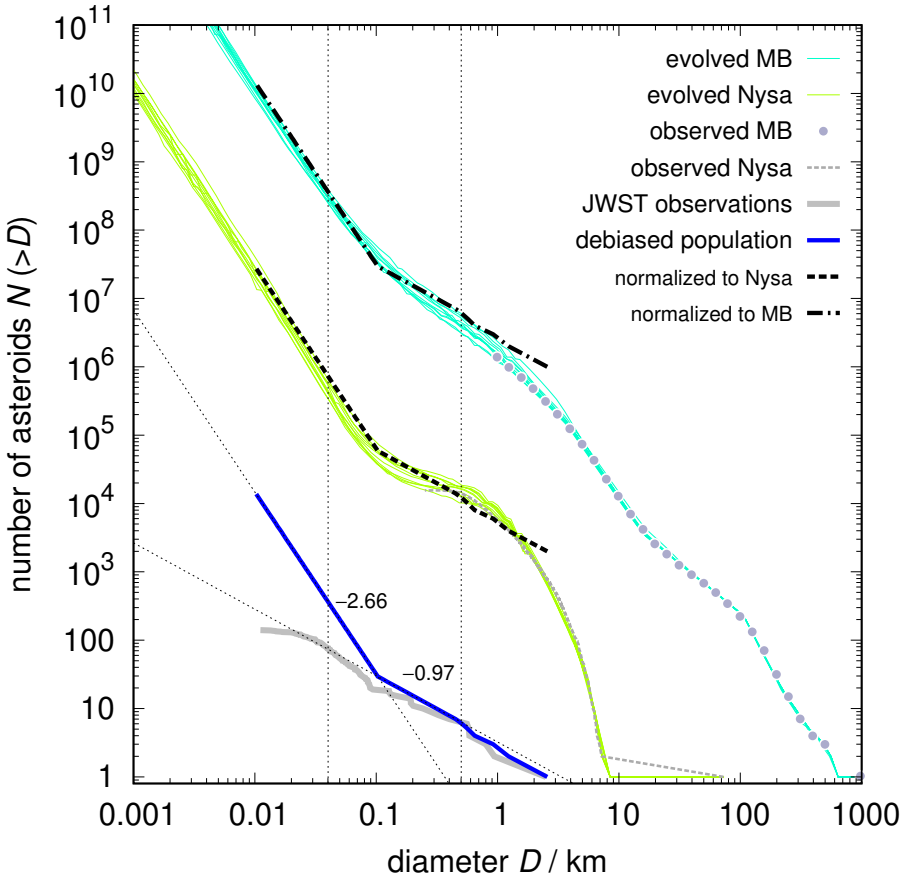

Figure 4: Asteroids observed by the JWST have a size-frequency distribution with a break at $\sim$100 m, revealing a population in collisional equilibrium. The observed (gray) and debiased (blue) cumulative SFDs, $N(>D) = CD^q$, are shown together with corresponding slopes q (dotted). According to the collisional model from ref. [13], this exactly corresponds to the main belt population between 1,000 and approximately 50 m (aquamarine). Additionally, evolved asteroid families exhibit similar exponents due to ongoing collisions with the main belt population. The Nysa family is plotted for comparison (lime), with a different normalization of the JWST data (dashed).

4 Methods

JWST image processing Data from Program IDs (PIDs) 1177 and 2304 were acquired with JWST/MIRI in October and November 2022 using FULL subarray mode resulting in $112'' \times 113''$ (1024×1032 pixels^2) FoV. Data from PID 3077 were obtained in November 2023 in BRIGHTSKY subarray mode resulting in a smaller FoV of $56.3'' \times 56.3''$ (512×512 pixels^2). All programs used F1500W filter and FASTR1 readout mode.

For our asteroid search, we downloaded exposure raw data products ("*uncal.fits" files) from the Barbara A. Mikulski Archive for Space Telescopes. Then, we ran Stage 1 and 2 JWST Science Calibration Pipeline version 1.13.4 to produce calibrated "*calints.fits" files. These files are single exposures containing results for all integrations in an exposure with world coordinates and photometric information. Every "*calints.fits" 3-D data file was sliced into a set of 2-D data files containing the pixel values for each integration with exposure time of 38.9 sec for PIDs 1177 and 3077, and 36.1 sec for PID 2304. For PIDs 1177 and 2304, we trimmed 2-D data files to exclude parts of the detector designed for coronagraphic imaging resulting in a useful FoV of $72'' \times 113''$ (654×1032 pixels^2). Each 2-D data file was then corrected for sky background using Photutils[53] Python software package. Background-subtracted images were then searched for any moving objects which happen to cross the FoV.

Detection of asteroids using synthetic tracking and their flux estimation We leveraged our custom-build wrapper[18,24] around the Tycho Tracker[54] synthetic tracking software to explore

a wide range of motion vectors and generating trial exposure stacks for each vector. No restrictions on position angle (PA) were used and speed was in a range of 0.001-1.2 arcsec/min. Our speed limits were set to enable detection of objects moving as slow as 0.5 pixel/hour and fast-moving objects streaking up to 10 pixels in a single integration. Each trial exposure stack was computed by shifting the exposures according to the motion offsets associated with the current vector. If an object had motion similar to that of the given vector, it was extracted from the trial exposure stack by the detection process. We grouped images to detect faster moving objects by dividing the image sequence from one JWST visit into overlapping groups of 100 exposures, ensuring the detection of an asteroid if it appears in at least 50% of the group's images. After detecting fast-moving objects, we performed a search for slower moving objects by searching all the images from one JWST visit (up to 350 exposures for PIDs 1177 and 2304, and up to 1000 exposures for PID 3077). A set of candidate detections (tracks) was returned with corresponding speed, PA, pixel coordinates, and SNR of detection.

We cross-matched every track with already known objects using the NASA Jet Propulsion Laboratory (JPL) Small-Body Identification Application Program Interface (API – `https://ssd-api.jpl.nasa.gov/doc/sb_ident.html`). A match was made if a known object was positioned within $0.1'$. We were able to detect 8 known asteroids and 138 unknown asteroids with SNR≥ 5 (see Extended Data Table 1 and Supplementary Table 1).

We measured the flux of each asteroid using aperture photometry, employing a circular

aperture with a radius of 2.5×FWHM (Full Width at Half Maximum) of the asteroids' point spread function (PSF) in the shifted and stacked image. The sky background was measured in an annulus beyond the asteroid aperture using a median sky fitting algorithm. The annulus had a radius of 4×FWHM and a width of 2×FWHM. We applied similar aperture photometry to estimate the flux of the TRAPPIST-1 star (the only stellar object in the FoV) and calculated the flux ratio of each asteroid to TRAPPIST-1. Previous studies[55] have shown that the absolute flux of TRAPPIST-1 in the F1500W band is stable at 2,590±80 μJy. We determined the absolute flux values of the asteroids using this reference flux of TRAPPIST-1. Flux estimates and their associated errors can be found in Extended Data Table 1 and Supplementary Table 1.

For the 15 asteroids crossing the PSF of TRAPPIST-1 or detector artifacts, we derived their fluxes based on several stacks of integrations that do not include crossing. We note that the same procedure of using multiple stack of integrations was used to check for flux consistency for all objects.

We do not perform color correction here as it is mostly constant between asteroids and thus does not affect the derived size-frequency distribution (our core finding). Color corrections for the MIRI bands were discussed in Ref.[15], and are needed because the spectral energy distribution of the reference (typically a calibration star, here TRAPPIST-1) is substantially different from the asteroids across the MIRI bandpass. For typical NEO and MBA temperatures between 200 and 400 K, these corrections are only 1% in the F1500W band. Only for very

distant objects (effective temperatures of 100 K or below) the required color correction would reach the 5% level. We thus omitted this correction, as the final diameter errors are dominated by the orbital uncertainties. Future studies targeting individual asteroid detection (rather than performing population studies–as done presently) will require such color corrections.

Asteroid detection efficiency We conducted a series of injection-recovery tests to evaluate our asteroid detection efficiency. We injected a 4×11 grid of synthetic moving objects, each with various flux values (see below), into 100 $72'' \times 113''$ (654×1032 pixels^2) FITS files from PID 1177. Synthetic objects were placed in such a way that they spend all the time (~ 1 hour) in FoV, had random PAs from a uniform distribution between 70 and 80 deg and random speeds sampled from an actual speed distributions of the detected objects (0.02-1.1 arcsec/min). Before running the synthetic tracker, we subtracted the sky-background. After completion of the synthetic tracking, we compared the detected objects with the injected ones. We repeated this test four more times for the same flux value as a sensitivity analysis for our estimated recovery rate as a function of flux. In total, we performed 11 sets of injection-recovery tests with objects having flux values of 3.5, 3.0, 2.5, 2.0, 1.5, 1.25, 1.0, 0.75, 0.5, 0.25 and 0.1 μJy. Our recovery rate is $\geq 80\%$ for objects down to $1.5\,\mu$Jy (see Extended Data Figure 1), which then drops to $50 \pm 2\%$ at $1.1\,\mu$Jy. The derived cutoff is 1.1 μJy with an observation bias starting at $\sim 1.5\,\mu$Jy (39 out of 138 unknown objects have fluxes smaller than $1.5\,\mu$Jy). This translates into an observational bias emerging in the 20- to 40-m diameter regime with a sharp cutoff by $\sim$10 m.

Regarding false positives, as seen in other asteroid search surveys, spurious associations of noise can coadd and lead to apparent signals that may be identified as possible detection[56,57]. Such noise patterns, however, typically manifest as a handful of bright pixels on the shifted and stacked image. In contrast, our confirmed detections exhibit tens of bright pixels arranged in a symmetric PSF, which is clearly distinguishable from the background (see Figure 1.b. and Supplementary Figure 1). To confirm that aspect, we selected a series of data cubes in which we detected objects and performed numerous random perturbations of the image time-stamps to assess if spurious associations of noise could lead to convincing false positives. Out of these dozens of random perturbations for five different observing epochs, none of the best detection candidates presented more than a handful of bright pixels arranged somewhat symmetrically, and thus look like the 138 detections showcased in Supplementary Figure 1. In addition, most of these spurious detections do not appear in both the first and second halves of the shifted and stacked images, a clear flag for a spurious signal.

Orbit estimations To estimate the sizes of the unknown asteroids from their IR fluxes, we require their positions at the time of observations with respect to the Sun and JWST (Observer), i.e. Observer-Target (O-T) distance, Sun-Target (S-T) distance, and the corresponding S-T-O phase angle. Due to the short duration of the asteroids' arcs in our data, a large ensemble of possible orbital configurations exist for each object—even in the case of the longest observing arc of 8 hours of unknown asteroid #91. To overcome this bottleneck, we developed a method using ensembles of orbital configurations of known objects that are present around JWST FoV

as proxies (or priors) to derive posterior probability distributions of O-T and S-T distances, and S-T-O phase angles for unknown asteroid distances. We assume that unknown asteroids must be related to faint known asteroids, because the former are fragments of bigger bodies (either released just after a break-up, or created by collisional cascade), i.e. they are genetically linked[13,14].

For every JWST visit, we obtained a list of all known asteroids predicted to be within a 6×2 degree^2 (RA$\times$Dec) reference field around the TRAPPIST-1 star using the JPL Small-Body Identification API. We queried JPL Horizons (`https://ssd-api.jpl.nasa.gov/doc/horizons.html`) for the speed, PA, O-T distance, S-T distance, and the corresponding S-T-O phase angles for each known asteroid. Then, every unknown asteroid was placed in speed/PA parameter space, and known objects in their proximity where used as proxies/priors to constrain their orbital configuration (Extended Data Figure 2).

We first used a series of ellipses to select proxies within a certain distance of each unknown object and test the sensitivity of the inferred properties. The proxy1s ellipse is defined as an ellipse with widths of 5% of the unknown object's speed and an absolute value 0.5 deg for PA (which correspond respectively to the typical 1-σ uncertainties on measured speed and PA by our pipeline). The proxy3s and proxy10s ellipses are $3\times$proxy1s's and $10\times$proxy1s's respectively. We assigned a distance to a particular unknown asteroid as a mean value of O-T distances to each proxy, i.e., known asteroids within different ellipses. We did similar calcula-

tions to S-T distance, and the corresponding S-T-O phase angles.

We assessed the sensitivity of our distance estimates to different sizes of the reference field around the TRAPPIST-1 star confirmed negligible dependencies when compared to the derived uncertainties (i.e., spread in O-T distance, S-T distance, and S-T-O angle). As a proof of concept, we tested this method on eight known asteroids observed at different epochs. We removed their true speed and PA values from the speed/PA parameter space and treated them as unknown objects. We found that in all instances, the proxy3s and proxy10s ellipses provide enough proxies to yield estimates within 1-σ of the true values—1-σ error bars are typically between 0.2-0.3 au. Extended Data Figure 3 shows an application of the method to the 8 known asteroids. All the known and derived properties of the 8 "validation objects" are reported in Extended Data Table 1.

While we observed that the proxy3s and proxy10s ellipses provide enough proxies to yield reliable estimates, we also observe that for a handful of known asteroids the proxy10s ellipses lead to substantially larger uncertainties due to a large number of proxies associated with different families joining the sample. In addition, we noticed that the approach aiming at using fixed ellipses in the PA,v space can lead to a large amount of discrepancies between the number of proxies returned for each object. In a final application of this proxy-based approach, we search for a convergence of both the estimated distances and the uncertainties on these distances by using the N closest proxies. We find that for all but asteroids $\#66$ and $\#106$, the values converge

and are stable when $10 \leq N \leq 25$ (example in Extended Data Figure 2.c). Below $\sim$10 proxies, small number statistics lead to biases on the estimated orbital configuration and related uncertainty. Above $\sim$25 proxies, we often start sampling other populations leading to artificially larger uncertainties (and often a small bias on the orbit estimation, drifting with increasing N). Regarding asteroids #66 and #106, these are flagged as possible NEOs (see Extended Data Table 2) which have very few close proxies and have, amongst the closest 25 proxies, one or more outliers which we remove manually to avoid biases. We present the example of asteroid $\#66$ in Extended Data Figure 2.d). Unknown asteroid $\#66$ is likely a NEO observed close to aphelion and has a limited number of close proxies. As a result, its 19^{th} and 20^{th} closest proxies are clear outliers (specifically Trans-Neptunian Objects, 2000 OJ67 and 2000 PN30),leading to a sudden jump of its derived uncertainty (blue curve). For all other asteroids, we use the 17 closest proxies under the label "proxy17n".

To complete our validation, we turned to a larger sample of known objects, randomly selecting a total of $\sim$20,000 known asteroids within the reference field across all epochs and assessing their distance through the "proxy17n". Doing so, we find that the median deviation between true distance and estimated distance is 0.007 au with a standard deviation of 0.24au. Considering the uncertainties associated with each individual proxy17n estimation (typically between 0.2-0.3 au, as mentioned above), this reveals an excellent match between the spread at the population level and the uncertainty at the level of individual estimates. We find that only 0.85% of the 20,000 asteroids have an estimated distance more than 3σ away from truth, which

is consistent with the distribution and small number statistics considering our main sample size (138). In addition, all of these outliers appear to be automatically flagged as outliers as their proxy17n distance estimates return large individual uncertainties (tapping into different populations).

Assessing the probable association of the unknown objects For each of the 138 unknown objects, we estimated their probable associations to individual populations. We used the same lists of known asteroids (proxies) close to the FoV, and plotted their proper orbital elements (semi-major axis $a_{\rm p}$, eccentricity $e_{\rm p}$, inclination $i_{\rm p}$). If most of the proxies for an object were located close to a known sizable family [19], we assessed this association as probable. We also verified the respective speed and PA of unknown asteroids. If they were too low, too high, or too offset with respect to typical values of main belt asteroids, the associations was either NEOs, Hildas, or Trojans. If the number of known objects was too limited or they were too scattered, we do not report any association. Our results are summarized in Extended Data Table 2.

On the expected population of near-Earth objects crossing the field of view In order to assess the sensitivity of this pencil-beam survey to the NEO population, we derived the fraction of NEOs in the 6×2 degree^2 reference field introduced in the previous section. We found that only 1.1% of all known objects predicted to be within the reference field at each observing epoch are NEOs. Given that we detect $\sim$130 MBAs, this means that $\sim$1.5 NEOs could be expected.

We used the derived PA and speed to assess for the probable association of each detection and found that up to 6 objects could be NEOs (see Extended Data Table 2). This difference is a natural consequence of the facts that (1) JWST/MIRI observations were done in mid-infrared making them sensitive to much smaller sizes (sub-km vs. decameter) as NEOs are hotter, and (2) the SFD of NEOs is steeper than the SFD of the MBAs due to the size-dependent transport. We thus consider our results to be consistent.

Debiasing asteroids' absolute magnitudes The size calculation of known asteroids relies on refined and debiased asteroids' absolute H-mag estimates, which were derived through a novel correction method *DePhOCUS*[58]. The method performs debiasing of astro-photometric observations from the MPC with corrections using a statistical analysis based on an accurate reference of 468 asteroids with more than 450,000 observations in total. The method allows a derivation of 17 updated significant color bands, 90 catalog and 701 observatory corrections (significance level $p = 0.90$), which lead to a reduction of more than 50% in the root mean square (RMS) of the asteroids' phase curve and a more accurate estimation of the parameters of the H-G phase curve model, where G is the slope parameter. We used the corrections to debias the observations at the MPC for all known asteroids in the present study and compute the absolute H magnitude values and their uncertainties, assuming $\mathrm{G} = 0.15$.

Size and albedo determination The radiometric analysis of all detected asteroids was done via the Near-Earth Thermal Model (NEATM[59]). NEATM was originally developed for near-Earth

asteroids, but is now also widely applied to asteroids in the main-belt and beyond (see, e.g. Ref.[60–62]). In this model, the asteroids are approximated by non-rotating and smooth spheres which are in instantaneous thermal equilibrium with the incident solar radiation. This allows to calculate the temperature of each surface element via $\mu \times (1 - A) \times S_{\rm sun}/r^2 = \epsilon\eta\sigma T^4$, where μ is the cosine of the angle between the element's normal and the direction towards the sun, A the bolometric Bond albedo, S_{sun} the solar incident energy at 1 au, r the heliocentric distance, ϵ the emissivity (a fixed value of ϵ=0.9 is taken), and σ the Stefan-Boltzmann constant. The infrared beaming parameter η was introduced as a free parameter. It can be determined from a fit to multi-band infrared measurements (as originally done in Ref.[59]), or calculated from published linear phase-angle relations (e.g., Ref.[60,62,63]). For specific asteroid groups average η values are often taken, e.g., η=1.4 for near-Earth asteroids[64], η=1.2 for Mars-crossing asteroids[61], η=1.0 for MBAs[60], η=0.77 for Hildas and Jupiter Trojans[65], or η=1.2 for Trans-Neptunian objects[66]. Ref.[60] also gave η-distributions for inner, middle, and outer main-belt objects, with peak values at around 0.95-1.1 for inner, 0.9-1.0 for middle, and 0.85-0.95 for outer main-belt asteroids. For the interpretation of our single-band data it is not possible to determine object-specific η-values from the measurements. Therefore, we took the η-relation by Ref.[62]: $\eta\ (\alpha)$ = 0.76 ($\pm$ 0.03) + (0.009 $\pm$ 0.001) deg^{-1}. This relation is based on the analysis of more than 5000 asteroids, all observed in two broad bands at 9 and 18 μm. As both bands are close to the MIRI F1500W band, we consider this solution as the most appropriate for our analysis. However, instead of the given parameter error, we use a more conservative η-error of $\pm$10% for the NEATM size and albedo calculations.

For very small asteroids (on the decameter scale) the NEATM model is not well tested. In addition, small objects tend to spin faster[67]. In this case, their surface temperature would be better described by the Isothermal Latitude Model (ILM) or Fast-Rotating-Model (FRM)[68] (see also discussions in Ref.[69]). We tested the impact of these model assumptions for the size calculation of typical main-belt asteroids. The smallest-size objects are only detected at small heliocentric distances $<$2.5 au and seen under phase angles between 20 and 30°. Assuming that such fast-rotating asteroids are nearly isothermal (modeled by a beaming parameter of 3.14 and lacking flux changes with phase angle), we find that the FRM-derived sizes are about 1.5-1.6 times larger then the default NEATM-derived sizes. However, the size and rotation-rate limits for the NEATM-to-FRM transition are not known. Ref. [70] found beaming parameters of 1-1.5 (very similar as in our NEATM calculations) for about 50 near-Earth objects with sizes between $\sim$8 m and about 100 m. Ref. [71] looked at the Yarkovsky semi-major axis drift rate of a rapidly rotating asteroid. They found an unexpectedly low thermal inertia, indicative for a highly porous or cracked surface. Both studies show no indications that fast-rotating decameter objects are predominantly isothermal and thus support the use of NEATM over FRM.

Although we recommend that future observations aim for immediate follow up of detections (within a few days) to place tight constraints on the orbit and are performed in a different MIRI band to inform the thermal and rotation properties of the detections, we note that the core result of our finding (namely, a steep SFD downward of $\sim$100 m) is independent from using NEATM or FRM. Indeed, using one or the other below a certain size primarily results in mul-

tiplying all sizes by a factor of $\sim$1.5 thereby keeping the SFD slope constant. In addition, that possible transition is expected at small sizes below our cutoff at $\sim$40 m for the slope estimate.

Properties of the eight known asteroids The errors in H-mag, η, and the measured flux are all considered in the NEATM calculations. An absolute flux error of 6% (10%) leads approximately to uncertainty of 3% (5%) for the size and 5% (9%) for the albedo, while the 10% higher (lower) η-value increases (decreases) the size. For these known asteroids, the dominating sources of uncertainty for the size estimates are the assumptions for η and the absolute uncertainty for the fluxes, while for the albedo, the large uncertainty in H-mag drives the final errors. Table 1 summarizes the NEATM input values and our findings for the eight known asteroids among the serendipitous detections.

Among all known asteroids, (194793) 2001 YP90 was observed by JWST continuously for the longest period of time (3 hours) and the data shows significant flux variations indicating an elongated body (see Extended Data Figure 4) with a minimum (maximum) flux of $550\,\mu$Jy ($1300\,\mu$Jy). These flux values translate into diameters of 640 ± 43 m (922 ± 70 m) and albedo values of $0.51^{+0.17}_{-0.14}$ ($0.24^{+0.10}_{-0.07}$). Calculated diameters at minimum and maximum flux are first order estimates for the elongation of the asteroid. Diameters and albedos reported in Table 1 were calculated using an average flux of 1.03 μJy. Obtained JWST light curve is in a good agreement with the data from ground-based telescopes (see section Follow-up observations).

Albedo values of asteroid 152630 (1997 GP4) derived from our radiometric analysis

($\mathrm{pV} = 0.29^{+0.12}_{-0.08}$) are in agreement with the expected value for S-type asteroids (0.26 ± 0.09[72]; see section Follow-up observations).

Out of the eight known MBAs, only (472944) 2015 GH28 has a published radiometric diameter. Ref.[60] used 11 W3-band measurements from the WISE/NEOWISE spacecraft (from 15/16 Feb 2010, at r_{helio}=2.45 au, Δ=2.23 au, α=23.8°, W3 band center at 12 μm) to derive a size of 2290$\pm$390 m, no albedo was determined. This is in good agreement with our findings.

Properties of the objects with unknown orbits For newly-detected objects we used the previously introduced population-driven constraints on their orbits (see method "Orbit estimations") to transform the measured F1500W fluxes into size estimates. As neither H-mag nor albedo are known, we simply determined a default NEATM size and took the unknown properties into account when we estimate the size error. The procedure is described by the following steps:

1. We use the calculated Observer-Target (O-T) distance, Sun-Target (S-T) distance, and the corresponding S-T-O phase angles from the 17 closest proxies ("proxy17n") for each object.

2. For each of the proxy17n geometries, we translated the measured flux into a radiometric size via the NEATM. The NEATM calculations are done for a geometric V-band albedo p_V = 0.15, and a beaming parameter η which is calculated for the specific S-T-O phase angle (see section "Size and albedo determination"). The corresponding 17 sizes (per

unknown object) are averaged.

3. The size error calculation take the following parameters into account: (a) standard deviation of the 17 proxy sizes (a typical 10% uncertainty on O-T translates into a 10% size uncertainty, the same is true for S-T); (b) absolute flux error (with a 10% flux error translating into a 5% size error); (c) additional 5% size error originating from the 10% accepted variation in the beaming parameter; (d) size error introduced by the unknown albedo: a p_V = 0.05 (0.30) object (in comparison with p_V = 0.15) would give a $\sim$2% larger ($\sim$3% smaller) size. The first 3 error contributions have a nearly Gaussian distribution and are added quadratically, the albedo component is added at the end in a linear way as we do not consider it an independent variable but rather account here uniformly for its whole range of possible value.

It is important to note that the derived size range for each object is dominated by the range of possible geometries, and for the low signal-to-noise ratio detections, also by the absolute flux error. The different assumptions for the albedos and the beaming parameter are almost negligible in the radiometric size determination. All the properties of the 138 new detections are reported in Supplementary Table 1.

For a validation of the method, we handled the 8 known asteroids in exactly the same ways as the 138 unknown ones. The resulting solutions are shown in Extended Data Figure 3 (based on S-T, O-T, and S-T-O values derived from the proxy17n's orbital properties). The

derived size ranges are very similar, and agree within the error bars very well with the solutions given in Table 1 where their true orbits were used. The asteroids are reported in the same order as in Extended Data Figure 3 and in Extended Data Table 1, i.e., asteroid #1 is 2011 SG255 and asteroid #8 is (472944) 2015 GH28.

Follow-up observations of the eight known asteroids We conducted ground-based follow-up observations of a set of known asteroids in our sample to better characterize their phase curve, colors, and rotation period and amplitude. Observations of (194793) 2001 YP90 and 2021 FR9 were acquired with the 1-m Artemis telescope[73] of the SPECULOOS network[74] and with the 0.6-m TRAPPIST-North[75] telescope. 2021 FR9 was observed between 2024 February 02-10 at solar phase angles ranging from 1.8° to 4.3°. The photometry and magnitude calibration to the Johnson V band was performed using the Photometry Pipeline[76]. 2001 YP90 was observed between 2024 February 01 and March 09 at solar phase angles ranging from 2.9° to 20.9° and included longer observation runs to determine its rotation period. We determined a period of 5.7701 ± 0.0001 h and a relatively large amplitude of 0.87 ± 0.10 mag, indicating an elongated body (Extended Data Figure 4).

A series of exposures with SDSS *griz* filters were also obtained for the asteroids 2001 YP90 and 1997 GP4 on February 16, with the 4.3-m Lowell Discovery Telescope (LDT, previously known as Lowell's Discovery Channel Telescope).[77] These spectro-photometric observations allowed to determine the taxonomic types for these two bright asteroids. For 2001 YP90

the taxonomic fits RMS values suggest that a K-type is the only good fit to the data. Derived values of albedo from our radiometric analysis (see section "Properties of the eight known asteroids") are also compatible with K-type asteroid. For 1997 GP4 asteroid, Sr-type is the best fit, but S- or Sq-types are close in terms of RMS (see Extended Data Figure 5).

On the information content and sensitivity of the size-frequency distribution Before interpreting the SFD, we assessed its sensitivity to uncertainties and biases in order to determine the size regime over which its information content can reliably be translated into scientific inferences. First, we developed a framework to adequately propagate the large uncertainties (Fig. 3.a.) on the asteroid sizes onto the SFD. To this end, we followed the Monte Carlo method[52] and generated an ensemble of 10,000 randomly perturbed diameters for each asteroid (Figs. 3.b., grey curves). As discussed in the previous section, the size uncertainties are primarily driven by the uncertainty on the orbital configuration (O-T and S-T each contribute at the level of $\sim$10-15%), in comparison to the contributions from the flux, beaming-parameter, and albedo uncertainties respectively contributing to a size uncertainty of $\sim$3-10%, $\sim$5%, and $\sim$2-4%. The probability distributions of the main variables/contributors (O-T, S-T, and flux) are found to follow Gaussian distributions. The probability distribution for the beaming parameter only marginally deviates from a Gaussian for the present application, while the albedo is best approximated by a uniform distribution between 0.05 and 0.30. The size uncertainty thus follows primarily a uniform distribution with an average relative standard deviation of $\sigma_D/D \sim 25\%$, where σ_D is the size uncertainty.

We note that due to the transformation from linear (sizes) to log (SFD) space, the uncertainty distribution on the SFD is asymmetrical. This means that the SFD derived from the median sizes does not correspond to the actual median SFD. Therefore, not accounting for the size uncertainties when deriving the SFD estimates can lead to biases when the size uncertainties are important (especially in the regime driven by large Gaussian uncertainties due to the wings of their distribution). In the present case, not accounting for the size uncertainty leads to an SFD estimate biased towards larger slope.

Similarly we note that it is pivotal to account for the expected distribution of uncertainties as well as the sample size when building the models to be compared with the SFD. Indeed, standard theoretical models are built assuming that a large number of asteroids are observed with an exquisite precision on their sizes, which is not true in practice. To highlight that aspect, we offer the following simple case: a theoretical population where all objects have the exact same size leading to a vertical SFD. Yet, any observation of this population will always return a spread of value due to uncertainties on each individual size measurements, which will result in a sloped SFD. That apparent slope will be dependent on the uncertainty on the size estimates, and the number of objects detected. Extended Data Figure 6.a. further develops this point by comparing the true slope of a SFD to its apparent slope as a function of the measurement uncertainty considering here uncertainty distributed primarily in a Gaussian fashion. It shows that for a regime where $\sigma_D/D \gtrapprox 15\%$ the apparent slope is systematically shallower. For the present study, it shows that the slopes of $q_S \sim -1.5$ and $q_B \sim -0.85$ respectively found for small

and big sizes (transition at $\sim$100 m, match with true (i.e., debiased) slopes of $q_{S,deb} \sim -2.66$ and $q_{B,deb} \sim -0.97$. We use this slope mapping to debias our SFD and match with theoretical models (Figure 4).

We note that for the size-uncertainty regime of this study, a wide range of true slopes match with the observed $q_S = -1.47 \pm 0.13$ (see Extended Figure 6.a.). This results in a posterior probability distribution on $q_{S,deb}$ substantially wider than $q_{B,deb}$ (respective spread: 0.60 vs 0.14, Extended Data Figure 6.b.). Future studies either increasing the number of detections and/or the orbital constraints (e.g., with a multi-visit follow-up strategy) will help reduce the uncertainties on the SFD, thereby allowing to disentangle between different families and study the source regions of meteorites[13,14,31] "in-situ".

We then investigated observational biases (or sensitivity limits). The first bias of observational origin relates to our detection threshold at $\sim$0.5 μJy. This threshold corresponds to a drop in recovery rate that emerges around 1.5 μJy and translates into an observational bias emerging in the 20- to 40-m diameter regime with a sharp cutoff by $\sim$10 m (Figure 3.a. and Extended Data Figure 1), meaning that the current SFD cannot readily be used beyond 40 m. On the other end of the size regime, large asteroids crossing the FoV are rare due to their lower occurrence rates. Therefore, the SFD derived from their detection is affected by small number statistics. To assess the size threshold above which this occurs, we generated synthetic populations of one million objects with exponents ranging from $q = -2.0$ to $q = -0.7$—$N(>D) = CD^q$—and

drew 10,000 random batches of 150 asteroids to assess the size regime over which the derived SFDs present an adequately small level of variance given our number of detections.

We find that the size cutoff for the sampling bias is dependent on the exponent, with a size cutoff ranging from 70m for $q = -2.0$ to 1200m for $q = -0.7$ (Extended Data Figure 6.c. and d.). Via a series of draws (e.g. Extended Data Figure 6.c.) and for different q exponents, we find that the best marker for identifying the size cutoff (i.e., when the slope starts diverging from the true slope) is $N \leq 7$. In other words, small number statistics is the best marker for this sampling bias at large sizes.

This finding also shed lights on the significant tension between the SFD estimate in the 40 to 100 m range and the number of "large" asteroids found ($N(>300\,\mathrm{m}) = 9$). Indeed, the likelihood of a sample of 150 asteroids with a $q = -1.45$ to also present $N(>300\,\mathrm{m}) = 9$ is roughly 1:10,000 (i.e., $\gtrapprox 4\sigma$). This provides additional support to the fitting of the SFD with a shallower slope beyond $\sim$100 m, where a transition is seen.

Interpretation of the size-frequency distribution Knowing which population has been sampled by our JWST observations is a key for an interpretation. According to Extended Data Figure 7, orbits of known faint objects located close to the JWST FoV are not evenly distributed across the main belt. Instead, they are associated to selected asteroid families, namely to Polana, Nysa, Massalia, Koronis2, or Karin, which are both populous and preferentially close to the ecliptic plane, similarly as the TRAPPIST-1 star. See Supplementary Table 1 for details.

The observed SFD of individual families are substantially different (e.g., Extended Data Figure 8). Some of them are steep down to the observational limit, which occurs at about 1,000 m, depending on the respective heliocentric distance and albedo. Others exhibit a distinct break at around $5,000\,\mathrm{m}$, below which the slope becomes shallower, with the exponent ~ -1.5, characteristic of a collisional equilibrium at km sizes. This is most likely the result of long-term collisional evolution of families.[13,14] In other words, young families (Massalia, Koronis2, Karin) have a steep SFD, while old families (Polana, Nysa, ...) have a shallow SFD at sub-km and decameter sizes.

5 Data and Code Availability

Data availability The data used here are publicly available on the Mikulski Archive for Space Telescopes (MAST) at the Space Telescope Science Institute (STScI), and are associated with programs 1177, 2304, and 3077 with Greene, Kreidberg, and Gillon as PI, respectively.

Processed JWST images used to create Figure 1 are available at Tycho Tracker website ("JWST TRAPPIST-1" dataset): `https://www.tycho-tracker.com/download`

Astrometric measurements of unknown asteroids are available in MPC isolated tracklet file (`https://sbnmpc.astro.umd.edu/MPC_database/statusDB.shtml`): tracklets AST001 – AST139, submission_ids (2024-08-06T23:54:21.000_0000GBYm, 2024-08-07T20:19:18.001_0000GBhr, 2024-08-07T22:38:47.000_0000GBiN, 2024-08-08T18:14:21.000_0000GBrb), where they will wait for the linking and confirmation from future, deep surveys.

Ground-based follow-up images are available by request.

Code Availability This work makes use of the following publicly available codes: NumPy[78], Matplotlib[79], Astropy[80,81], SciPy[82], Pandas[83,84], Astroquery[85].

6 Acknowledgments and Author Contribution

Acknowledgments The authors thank Dr. Peter Veres and Dr. Matthew Payne from the Minor Planet Center (MPC) for their timely support in enabling the processing of these JWST asteroid detections by MPC. This work is based in part on observations made with the NASA/ESA/CSA JWST. The data were obtained from the Mikulski Archive for Space Telescopes (MAST) at the Space Telescope Science Institute (STScI), which is operated by the Association of Universities for Research in Astronomy, Inc., under NASA contract NAS 5-03127 for JWST. These observations are associated with programs 1177, 2304, and 3077 with Greene, Kreidberg, and Gillon as PI, respectively. A.Y.B. and J.d.W. thanks Michael J. Person for discussions regarding astrometry and Scott Stuart for initial SFD calculations. J.d.W. and MIT gratefully acknowledge financial support from the Heising-Simons Foundation, Dr. and Mrs. Colin Masson and Dr. Peter A. Gilman for Artemis, the first telescope of the SPECULOOS network situated in Tenerife, Spain. This work has been supported by the Czech Science Foundation through grant 21-11058S (M. Brož). This work has been supported by the NVIDIA Academic Hardware Grant Program. TRAPPIST is funded by the Belgian National Fund for Scientific Research (F.R.S.-FNRS) under grant PDR T.0120.21, and the university of Liège. E.J. is a Belgian FNRS Senior Research Associate. T.H. gratefully acknowledges financial and technical support from ESA, the Erasmus+ program, co-funded by the European Union, and the Cusanuswerk Bischöfliche Studienförderung, funded by the German Federal Ministry of Education and Research.

Author Contributions A.Y.B. and J.d.W. designed and led the study. A.Y.B. performed the data reduction and asteroid detection (incl., injection-retrieval tests) following Ref.[18] with support from J.d.W.. J.d.W. designed the population-based distance estimation with support from A.Y.B., provided the preliminary size estimations, and performed the information-content analysis for the size-frequency distribution with support from M.B. M.B. performed the interpretation of the size-frequency distribution. T.G.M. derived the final size and albedo estimates. T.H. provided the debiased H magnitudes. EJ put in relation the exoplanet team with asteroids experts and led the ground based follow-up observations together with A.Y.B., M.F., W.M.G., T.K., N.M., A.T., and C.A.T. M.F. led the rotation curve analysis. M.M. provided the detailed orbital estimations. D.P. and S.N.H. provided complementary target identifications, flux estimates, and support for Tycho Tracker. R.P.B. contributed to the early interpretation of the results. E.D., L.K., M.G., T.P.G., P.-O.L., and S.Z. led the JWST observation programs of TRAPPIST-1 behind these serendipitous asteroid detections. All authors contributed to the writing of the manuscript.

Competing Interests The authors declare that they have no competing financial interests.

Correspondence Correspondence and requests for materials should be addressed to jdewit@mit.edu.

7 Extended Data

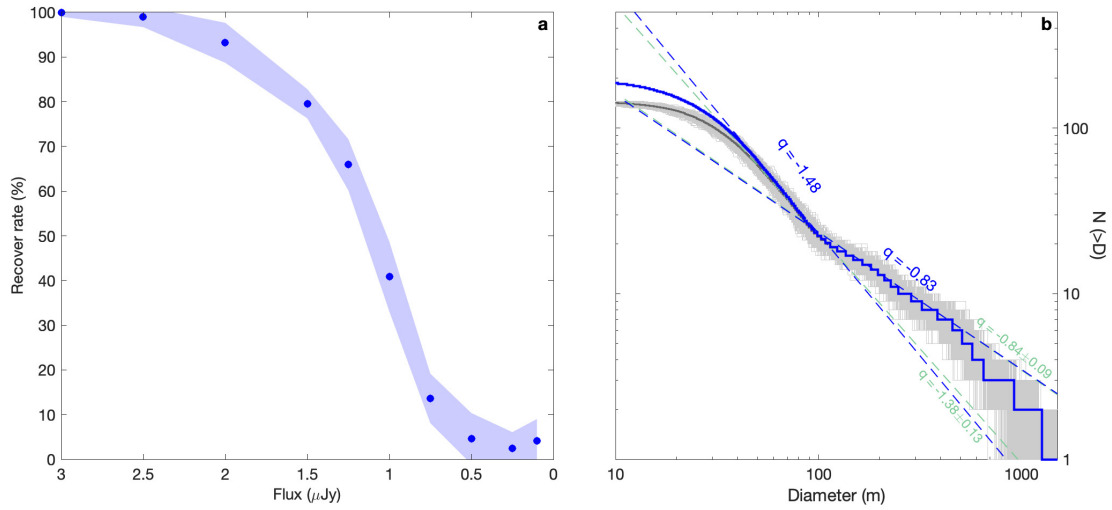

Extended Data Figure 1: Completeness test and recovery rate. a. Fraction of recovered synthetic asteroids as a function of their flux based on injection-recovery tests to assess the completeness of our search and correct the derived size-frequency distribution. The shaded area represent the 1-σ deviation from the reported rates seen across a range of injections. The derived cutoff is 0.5 μJy with a observation bias starting at $\sim$ 1.5 μJy (i.e., at the 20- to 40-m size regime). **b.** Ensemble of cumulative size-frequency distributions (SFDs) built from 1,000 perturbed asteroid diameters in order to propagate the size uncertainties onto the SFD estimate (median in grey) via the Monte Carlo method[52] together with the SFD debiased for brigthness-dependent recovery rate (blue).

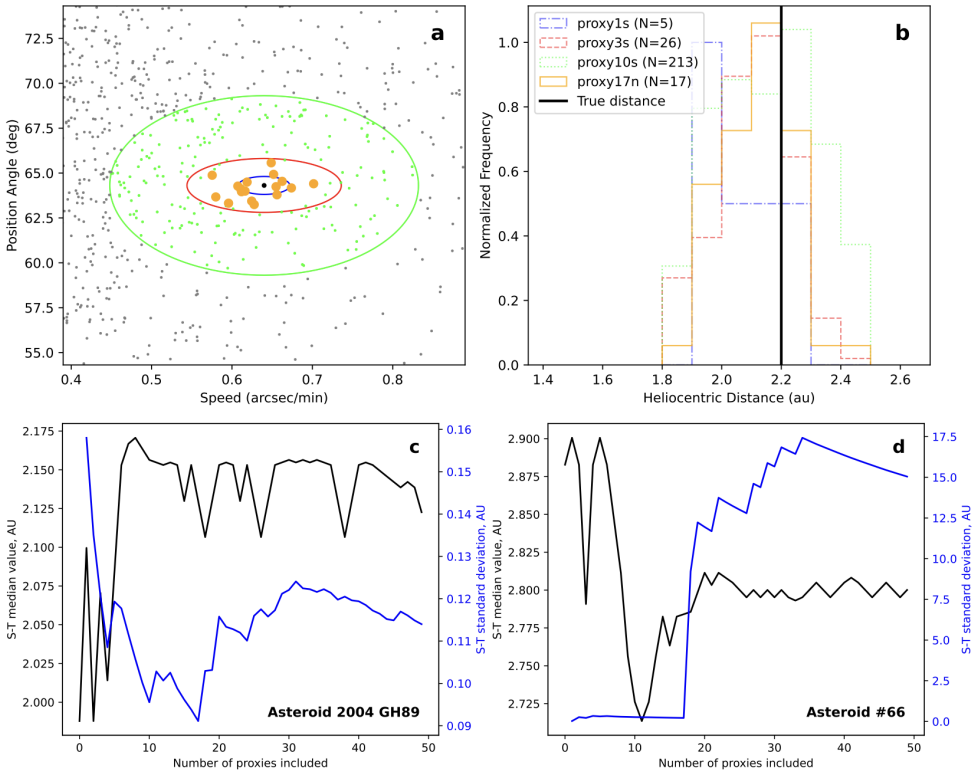

Extended Data Figure 2: Proof-of-concept application of population-based estimation of a distance to an asteroid a. Speed (v) and position angle (PA) of asteroid 2004 GH89 (black dot) compared to an ensemble of other known asteroids close to the field of view at the time of the observation (grey dots) together with proxy1s, proxy3s, and proxy10s ellipses (blue, red, green) used to select neighbors/proxies and the final 17 "proxy17n" proxies used (orange). **b.** Histogram of heliocentric distances (S-T) of from the different ensembles of proxies compared to the true value (black line) confirming that with an increasing number of proxies (N) the derived orbital configuration converges towards truth. **c.** Estimated heliocentric distance (black) and its uncertainty (blue) for asteroid 2004 GH89 as a function of N. For $N << 10$, small number statistics can bias the derived distance and yield an artificially large associated uncertainty. Beyond $N \sim 20 - 25$, more proxies present new/different orbital configurations resulting in sudden changes in the estimated value (otherwise converging) and thus a progressive inflation of the estimated uncertainty. **d.** Same as **c.** but for unknown asteroid #66 (likely NEO) with a limited number of close proxies leading to its 19^{th} and 20^{th} closest proxies to be clear outliers (TNOs) resulting in a sudden jump of its derived uncertainty.

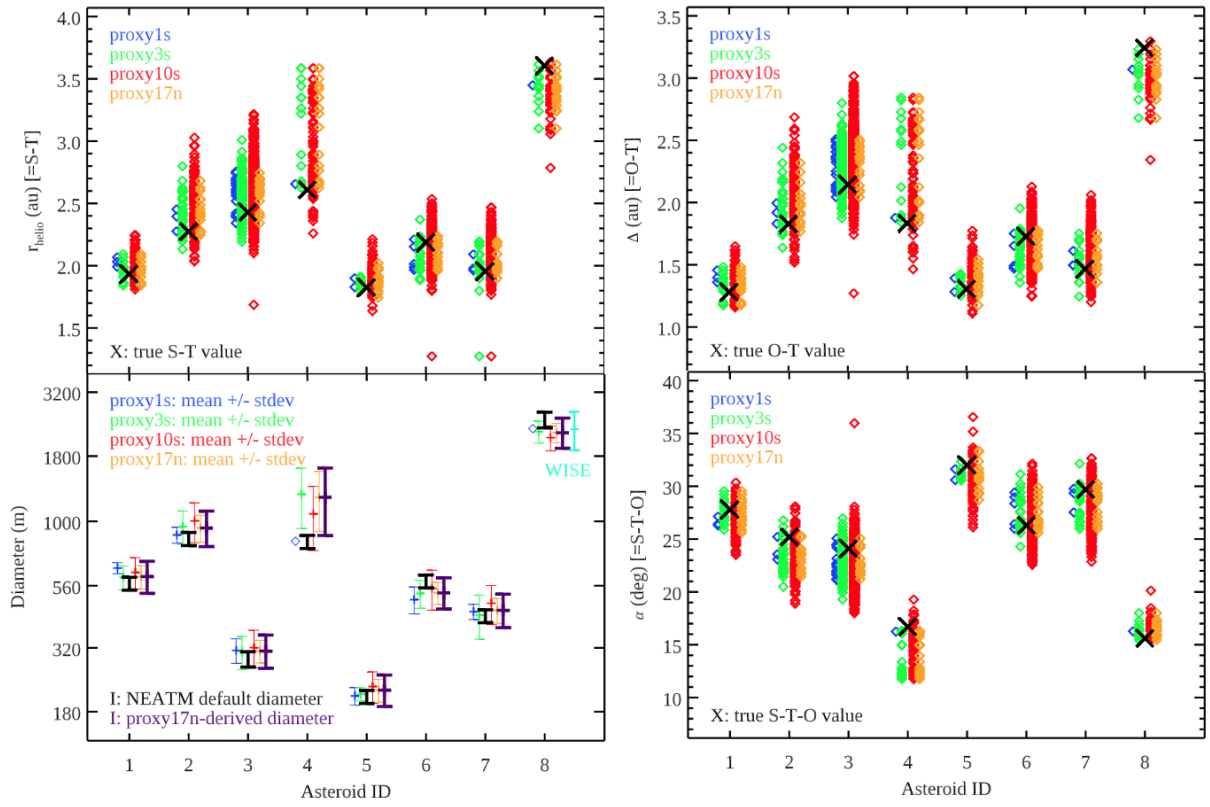

Extended Data Figure 3: Proof-of-concept application of the population-based orbit derivation for the eight known asteroids. (Left) Derived heliocentric distance for the eight known asteroids based on the proxy1s, proxy3s, proxy10s, and proxy17n neighbors (blue, red, green, orange) and the same for the radiometric diameter inferred from the population-based heliocentric distance versus true orbit. Asteroid #8 has a measured size which is reported in cyan. (Right) Derived distance from JWST to the eight known asteroids and corresponding Sun-Target-Observer (S-T-O) phase angles. For all proxy3s, proxy10, and proxy17n estimates for the distances—which are based on a large enough (i.e., statistically relevant) number of proxies, the existing size and phase angles agrees to within 1-σ supporting the reliability of the methodology used. See asteroid names in Extended Data Table 1 where they are reported in the same order (i.e., asteroid #1 is 2011 SG255 and asteroid #8 is (472944) 2015 GH28).

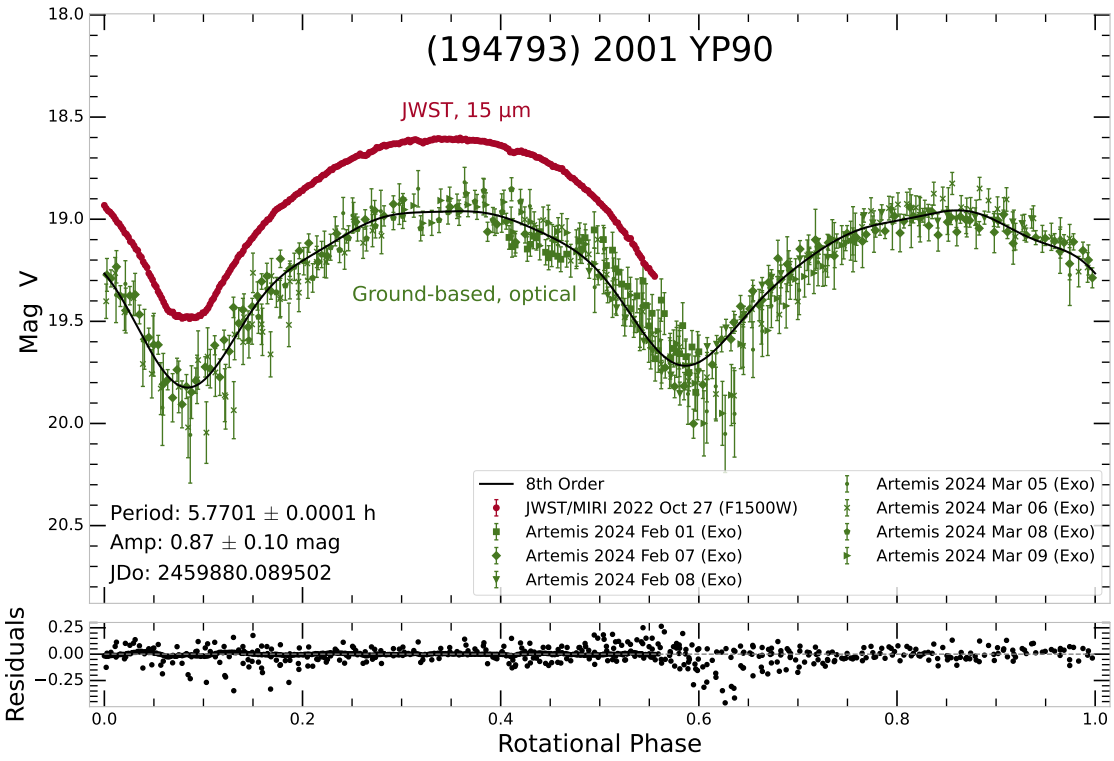

Extended Data Figure 4: Phased rotational lightcurve of 2001 YP90. Photometric observations of 2001 YP90 obtained with the Artemis telescope[73] (in green) indicate a rotation period of 5.7701 ± 0.0001 h and an amplitude of 0.87 ± 0.10 mag. The red curve corresponds to the MIRI observations shifted to the V band data (-0.35 mag for clarity) and shows a very good match with the optical observations in shape and amplitude. The MIRI data uncertainties are plotted but are smaller than the markers size.

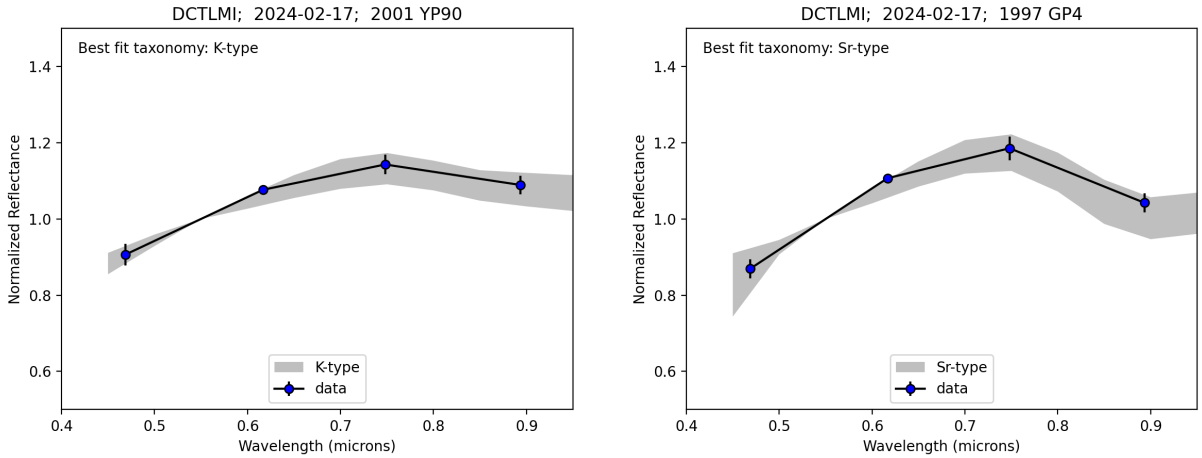

Extended Data Figure 5: Spectro-photometric taxonomic types of bright asteroids 2001 YP90 and 1997 GP4. Data were obtained with SDSS *griz* filters. Best-fit taxonomic types were determined based on minimizing RMS residuals between the data and re-sampled templates of taxonomic types in the Bus-DeMeo system. The albedos inferred from our radiometric analysis are in agreement with the ones from taxonomic classifications.

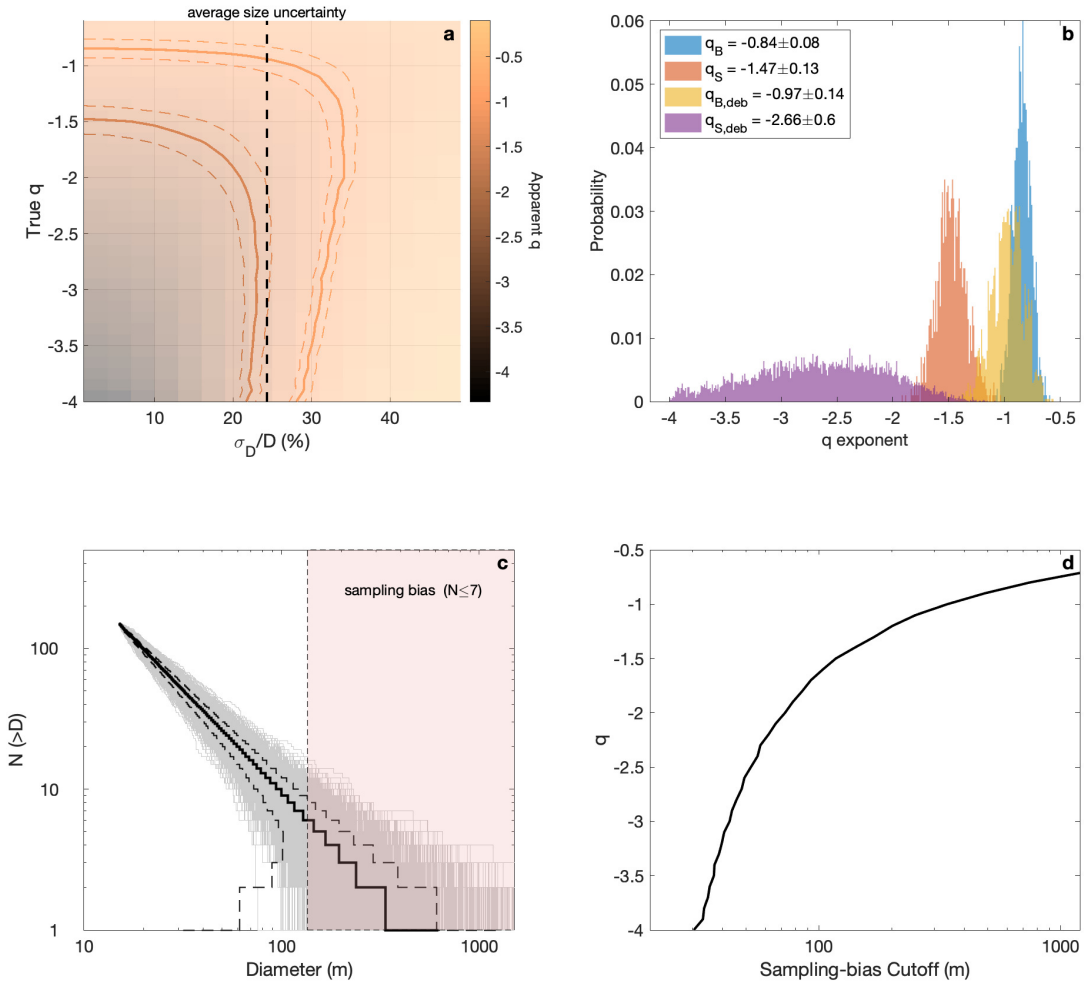

Extended Data Figure 6: Information content and sensitivity analysis of a size-frequency distribution. a. True versus apparent q exponent for ensembles of 1,000 samples of 150 asteroids drawn from a synthetic family, as a function of the relative size uncertainty (σ_D/D). Apparent slopes are consistently shallower as "smoothed out" by size measurements following primarily a Gaussian distribution. The contours represent the $q_S = -1.47$ and $q_B = -0.84$ slopes observed, which match true/debiased slopes of $q_{S,deb} \sim -2.66$ and $q_{B,deb} \sim -0.97$ for our average size uncertainty (dashed line). **b.** Posterior probability distributions for the observed q exponents in the small- and big-size regimes (q_S and q_B, respectively below and above the transition at ∼100 m) and their debiased estimates ($q_{S,deb}$ and $q_{B,deb}$). **c.** SFDs from 3,000 random draws of 150 asteroids from a $q = -1.45$ population of ∼1e6 asteroids showing consistent slopes until ∼130m due to small-number statistic ($N \leq 7$), the "sampling-bias cutoff". **d.** Relationship between the sampling-bias size cutoff and the q-coefficient of a population for a sample size of 150 asteroids.

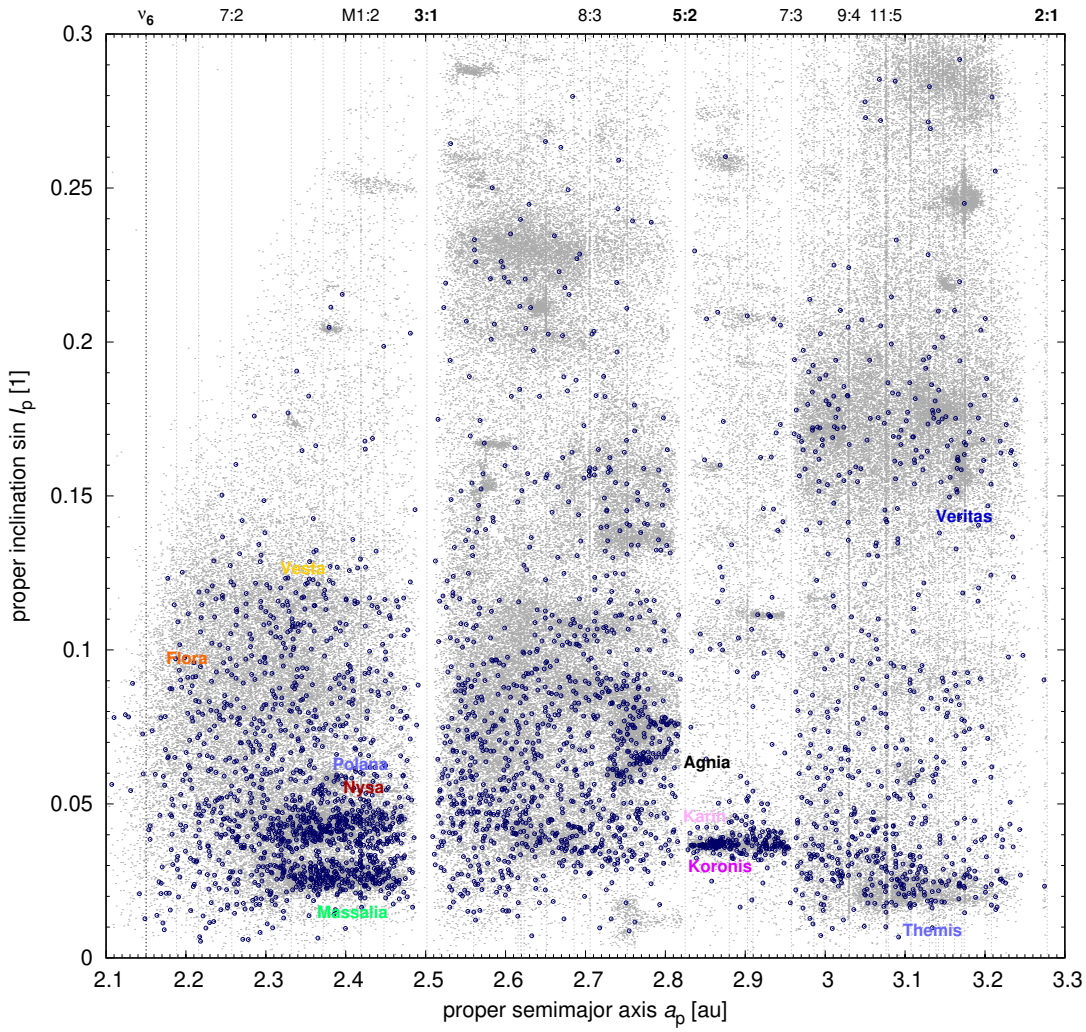

Extended Data Figure 7: Orbital elements of known asteroids located close to the field of TRAPPIST-1. All these asteroids had a similar speed and position angle as the unknown asteroids observed by the JWST. Their proper semimajor axis $a_{\rm p}$ versus the proper inclination $\sin i_{\rm p}$ (blue circles) is compared to other faint main belt asteroids observed by the Catalina Sky Survey[86] (gray dots). Their concentrations ('clouds') correspond to known asteroid families [19]. Sampling is non-random due to the geometry of JWST observations. Preferentially, the Nysa, Polana and Massalia families are sampled, together with other families at low inclinations (Koronis2, Karin).

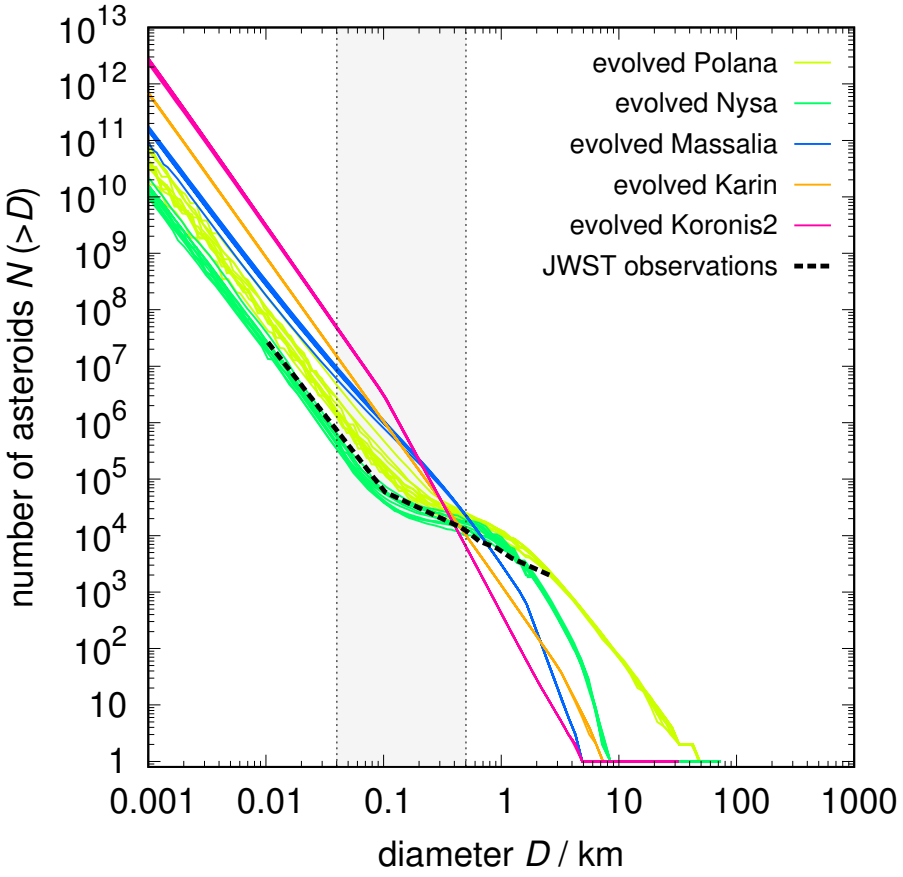

Extended Data Figure 8: Young and old asteroid families have very different size-frequency distributions between 1,000 and 50 m. A comparison of synthetic distributions of asteroid families from refs. [13,14,31] shows that prominent young families (Massalia, Koronis2, Karin) commonly have a steep slope (the exponent $q \simeq -2.5$ up to -4), while old families (Polana, Nysa) have a shallow slope ($q \simeq -1$ to -1.5). This difference stems from the fact that hundred-meter-size bodies are the weakest bodies in terms of their strength (i.e., energy per unit of mass needed for disruption) [30]. Consequently, their collisional evolution is so substantial that after approximately 100 My the exponent changes dramatically [13].

Extended Data Table 1: Properties of the eight known asteroids. H_{fit} reports the estimated V-band H magnitudes, r_{helio} the heliocentric distances, Δ the JWST-centric distance, α the phase angle, η the infrared beaming parameter, D the diameters, and p_V the geometric V-band albedo.

Name	H_{fit}(*)	r_{helio}(au)	Δ(au)	α	η(**)	flux(μJy)(***)	D (m)	p_V
2011 SG255	19.28	1.9328	1.2798	27.8	1.01	1,660$\pm$100	571$\pm$33	$0.105\pm^{0.034}_{0.027}$
(152630) 1997 GP4	17.09	2.2750	1.8284	25.2	0.99	1,240$\pm$74	854$\pm$50	$0.353\pm^{0.099}_{0.084}$
2021 FR9	19.32	2.4289	2.1444	24.1	0.98	90$\pm$9	289$\pm$20	$0.395\pm^{0.108}_{0.092}$
(194793) 2001 YP90	17.32	2.6092	1.8337	16.7	0.91	1,030$\pm$62	832$\pm$49	$0.302\pm^{0.086}_{0.073}$
2013 PG137	20.37	1.8259	1.3056	32.0	1.05	200$\pm$12	206$\pm$12	$0.295\pm^{0.086}_{0.071}$
2004 GH89	18.15	2.1869	1.7275	26.3	1.00	710$\pm$43	583$\pm$34	$0.286\pm^{0.082}_{0.069}$
2016 UR72	18.83	1.9551	1.4658	29.7	1.03	620$\pm$37	426$\pm$25	$0.286\pm^{0.084}_{0.069}$
(472944) 2015 GH28	16.66	3.6049	3.2427	15.6	0.90	1,630$\pm$163	2,497$\pm$177	$0.061\pm^{0.020}_{0.015}$

Notes. (*) We assume a $\pm$0.3 mag error for the radiometric size-albedo calculation.

(**) The η values were calculated via the η-relation given above [62], but we allow for a $\pm$10% uncertainty (which translates into an additional 5% uncertainty in the diameter calculation and an additional 10% in the albedo calculation) . The calculated minimum (maximum) η values for the 8 asteroids are 0.81 (1.15).

(***) The detections of the known asteroids have all very high SNRs, but for the size-albedo determination we took an absolute flux error of 6%, covering the MIRI imaging flux calibration, color corrections (between the stellar and the asteroid SEDs), and MIRI signal drift uncertainties. For the asteroids #03 (flux below 100 μJy) and #08 (located in the coronographic part of the MIRI detector) we increased the flux error to 10%.

Extended Data Table 2: Probable associations of 138 unknown asteroids detected by the JWST to individual populations. According to the measured proper motions and position angles, most of them belong to main-belt families, only a few to NEOs, Hildas, Trojans.

1	Themis?
2	
3	
4	
5	
6	
7	high-inclination
8	Polana
9	
10	Nysa
11	
12	Veritas
13	Nysa, Massalia
14	Nysa, Massalia, Karin
15	Nysa, Polana
16	NEO?
17	Massalia, Themis
18	Themis?
19	Massalia
20	
21	
22	Vesta?
23	Massalia, Nysa
24	Massalia
25	
26	Veritas?
27	Flora, Vesta
28	Vesta?
29	
30	Veritas?
31	Massalia, Nysa, Polana, Karin
32	Veritas?
33	Massalia, Nysa, Polana, Karin
34	
35	Themis
36	
37	
38	Massalia, Nysa
39	
40	NEO?
41	Vesta?
42	
43	
44	Massalia, Nysa, Polana, Karin
45	high-inclination
46	Themis
47	
48	
49	
50	
51	Nysa
52	high-inclination
53	Nysa, Polana
54	
55	
56	
57	
58	Massalia?
59	NEO?
60	
61	
62	Nysa?
63	
64	
65	
66	
67	
68	
69	Massalia
70	
71	
72	
73	
74	
75	Nysa?
76	
77	NEO?
78	
79	Nysa, Massalia
80	Hilda?
81	Massalia?
82	Veritas?
83	Massalia, Nysa, Polana, Karin
84	high-inclination
85	Massalia, Nysa
86	Massalia, Nysa, Polana, Karin
87	Nysa, Massalia, Karin
88	Nysa, Massalia
89	Polana?
90	
91	Trojan
92	Veritas?
93	Veritas?
94	high-inclination
95	Massalia, Nysa
96	Massalia, Nysa, Karin
97	Nysa, Massalia, Karin
98	Massalia, Nysa, Koronis
99	Flora
100	high-inclination
101	
102	Nysa, Massalia, Karin
103	Nysa, Massalia
104	Flora?
105	Flora
106	NEO?
107	Nysa, Massalia, Karin
108	Massalia, Nysa
109	Themis
110	Nysa?
111	Massalia, Nysa
112	Massalia, Nysa
113	Massalia, Nysa
114	Nysa, Massalia, Polana, Karin
115	Flora, Vesta?
116	Massalia, Polana
117	Nysa, Massalia, Polana, Karin
118	Nysa, Massalia, Polana, Karin
119	Massalia, Nysa, Karin
120	Massalia?
121	Massalia?
122	Veritas?
123	Nysa, Massalia, Polana, Karin
124	Massalia, Polana
125	Polana?
126	Flora?
127	Nysa, Massalia
128	Vesta?
129	Flora?
130	Massalia
131	Massalia
132	Nysa, Massalia, Polana
133	Vesta?
134	Vesta?
135	Agnia?
136	NEO?
137	Nysa, Massalia, Polana, Karin
138	Flora?
139	Massalia, Nysa

Supplementary References

Supplementary Figure 1 Portrait gallery of the 138 new asteroids detected. We note that index #47 is skipped as it appeared to be a duplicate of #54. We kept subsequent index up to 139 to match the indexing in our accepted MPC submissions.

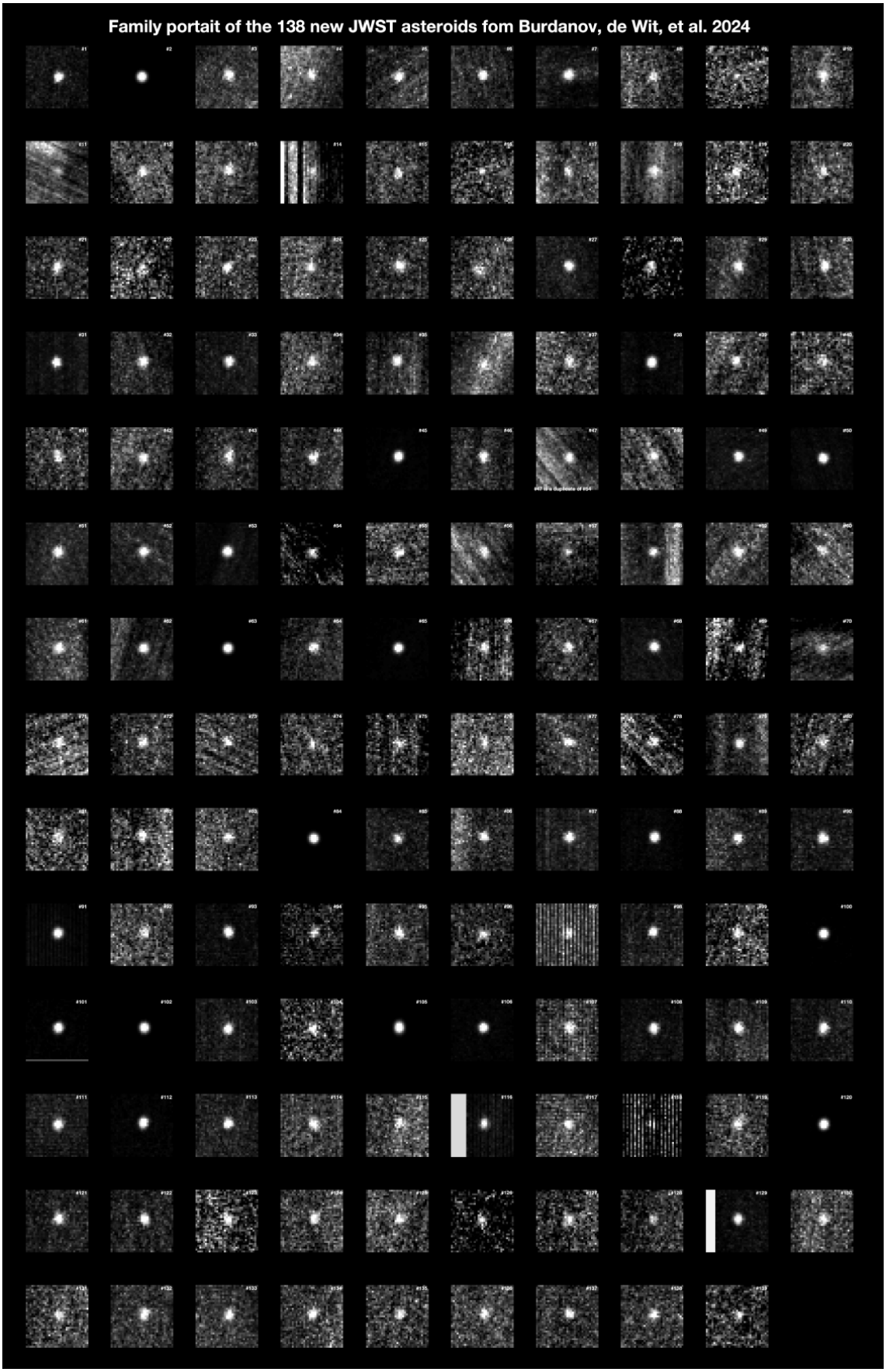

Overiew of the Supplementary Figure 1 Supplementary Figure 1 presents a series of snapshot of the 138 detections of unknown asteroids by JWST presented here.